American Mineralogist, Volume 109, pages 709–728, 2024

Revisiting the genesis of the adakite-like granitoids in collisional zones: Water-fluxed melting of intermediate to felsic rocks with dilution by low Sr/Y phases

Yuan-Hui Xie[1], Joshua J. Schwartz[2,†], Xiao-Wei Li[1,*], Keda Cai[1,*], Bader Thomas[3], Huan Li[4,‡], Fang-Yue Wang[5], Xiao-Bing Zhang[6,§], Xuan-Xue Mo[1], and Guo-Chen Dong[1]

[1]State Key Laboratory of Geological Processes and Mineral Resources, and School of Earth Sciences and Resources, China University of Geosciences, Beijing 100083, China
[2]Department of Geological Sciences, California State University Northridge, Northridge, California 91330, U.S.A.
[3]School of Earth and Space Sciences, Peking University, Beijing 100087, China
[4]Key Laboratory of Metallogenic Prediction of Nonferrous Metals and Geological Environment Monitoring, Ministry of Education, Central South University, Changsha 410083, China
[5]Ore Deposit and Exploration Centre, Hefei University of Technology, and School of Resources and Environmental Engineering, Hefei University of Technology, Hefei, 230009, China
[6]State Key Laboratory of Isotope Geochemistry, Guangzhou Institute of Geochemistry, Chinese Academy of Sciences, Guangzhou 510640, China

Abstract

High-Sr/Y granitoids in continental settings are sometimes erroneously regarded as the products derived from partial melting of thickened/delaminated mafic lower curst under relatively higher pressures (>1.5 GPa) in a collisional orogenic setting. In fact, multiple magmatic processes in the *trans*-crustal magma system, such as recycling of antecrysts, crustal assimilation, and fractional crystallization, can create or modify the primary "adakitic" signature. As a result, the generation of adakitic magmas in continental settings remains controversial from a bulk-rock perspective. Here, we address the origin of adakitic plutonic rocks through geochemical and textural characterization of rock-forming minerals in the pyroxene-bearing Zhuyuan granodiorite, West Qinling, China. The Zhuyuan granodiorite formed in a post-collisional setting and primarily consists of resorbed orthopyroxene, three types of clinopyroxene, amphibole, two types of plagioclases, K-feldspar, biotite, and quartz. Type-1 Cpx has high X_{Mg} (70.0–81.7). Type-2 Cpx displays normal zoning and decreasing X_{Mg} (80.9 to 71.5) from the core to rim. Type-3 Cpx is reversely zoned, where the rims have higher X_{Mg} (75.5–86.9), Ni, Cr, suggesting a recharge event. Orthopyroxene has high-Ni and -Cr contents, as well as high X_{Mg} (80.9–82.8), indicative of antecrysts that grew in mafic magma reservoirs. The injection of magmas from different sources is supported by sieve-textured plagioclase and crystal size distributions of non-poikilitic amphibole. Finally, non-sieve textured plagioclase, biotite, K-feldspar, and quartz are late-crystallized phases, indicative of an orthocrystic origin. The melts in equilibrium with these orthocrysts display significantly higher Sr/Y values than the magma batches that crystallized other mafic phases (i.e., amphibole, clinopyroxene, and orthopyroxene). Thus, we propose that the system involved an initial high-Sr/Y melts in equilibrium with the orthocryst assemblage was generated by water-fluxed melting of intermediate to felsic sources. The addition of low Sr/Y non-orthocrysts (e.g., amphibole and pyroxene) and associated melt diluted the original "adakitic signal" in the magma reservoir and drove the bulk composition to more mafic values. Consequently, the Zhuyuan pyroxene-bearing granodiorite represents a mixture of crystals with diverse origins and distinct magma batches of various compositions (from felsic to mafic compositions). Our study emphasizes that the origin of adakitic granitoids cannot be clearly deciphered without geochemical analysis of the constituent minerals. We also suggest that Sr/Y values in plutons should be cautiously used in paleo-crustal thickness estimates in collisional settings because of possible open system scenarios as described here.

Keywords: Adakitic rock, antecryst, dilution, pyroxene-bearing granodiorite, water-fluxed melting

Introduction

The term "adakite" was originally defined as high-Mg andesites produced by the partial melting of subducted oceanic crust (Kay 1978; Defant and Drummond 1990). Geochemically, adakites are characterized by elevated Sr contents (>400 ppm), high-Sr/Y and -La/Yb values, but depleted Y (<18 ppm) and HREE (e.g., Yb <1.8 ppm) (Defant and Drummond 1990). Several mechanisms have been proposed for the origin of adakitic magmas based on whole-rock geochemical compositions (Ma et al. 2015; Shen et al. 2021 and references therein). For example, primary magmas with adakitic affinity may be generated by partial melting of various sources under various pressures [e.g., delaminated lower crust, thickened lower crust, mantle wedge peridotite metasomatized by slab melts, intermediate to felsic source rocks with initially high Sr, low Y and Yb (Calmus et al. 2003; Moyen 2009; Ma et al. 2015; Ji et al. 2018; Ou et al. 2017; Yu et al. 2015; Zhan et al. 2020)]. On the other hand, magma processes (e.g., fractional crystallization, crystal accumulation,

* Co-corresponding authors E-mail: xwli@cugb.edu.cn, Orcid 0000-0002-6373-2159; caikd@cugb.edu.cn, Orcid 0000-0003-4004-9530
† Orcid 0000-0002-8385-2705
‡ Orcid 0000-0001-5211-8324
§ Orcid 0000-0003-2148-9442

0003-004X/24/0004–709$05.00/DOI: https://doi.org/10.2138/am-2022-8873

and/or magma mixing) may produce or modify "adakitic" felsic melts (e.g., Chen et al. 2016; Guo et al. 2007). For example, amphibole fractionation prior to plagioclase saturation would lead to the enrichment of Sr and depletion of Y in derivative melts (Moyen 2009; Nandedkar et al. 2016). As such, the origin of adakites has been controversial, and this issue warrants further reevaluation via comprehensive mineral-scale geochemical investigation (Castillo 2012; Castillo et al. 1999).

Moreover, previous reported mechanisms for the generation of adakitic magmas were largely based on experiments and modeling using a simple rock source or a melt-dominated closed system (e.g., Martin et al. 2005; Stern and Kilian 1996); however, recent crystal population studies on *trans*-crustal magma-mush reservoirs have challenged the suppositions necessary to generate adakitic magmas especially in plutonic arc crust (e.g., Paterson et al. 2016; Graham et al. 2020; Brackman and Schwartz 2022). For example, some workers argue that felsic magma reservoirs likely comprise multiple generations of crystals [e.g., orthocrysts, antecrysts, peritectic crystals, or xenocrysts (Bach et al. 2012; Miller et al. 2007; Clemens and Stevens 2012)] of contrasting origins (Jerram et al. 2018; Miller et al. 2007), which are entrained by different batches of both interstitial melts and volatile phases [i.e., a system of melt stored in a framework of crystals, referred to as crystal mush (Cashman et al. 2017; Collins et al. 2020; Wieser et al. 2020)]. In some cases, original adakitic signals (i.e., high-Sr/Y and -La/Yb values) could be diluted by the addition of non-orthocrysts characterized by low Sr/Y values (e.g., Macpherson et al. 2006), and as a consequence, geochemical trends defined by the whole-rock compositions could deviate from the liquid line of descent of the host magma due to the addition of various proportions of non-orthocrysts.

One approach to characterize these complex geochemical signals is to determine the compositions of individual minerals such as plagioclase, pyroxenes, titanite, zircon, and apatite, which have become widely used as petrogenetic tools in supplementing or even replacing conventional bulk-rock analyses. For instance, Hollings et al. (2020) used early-crystallized apatite to show that the "adakite signal" of the equilibrium melt had not been influenced by subsequent amphibole-dominated fractional crystallization. In this regard, geochemical signatures of constituent minerals that witnessed different stages of the geochemical evolution history and/or various sources may provide new perspectives for further constraining mechanisms of adakites generation.

Here, we explore the Late Triassic post-collisional grano-

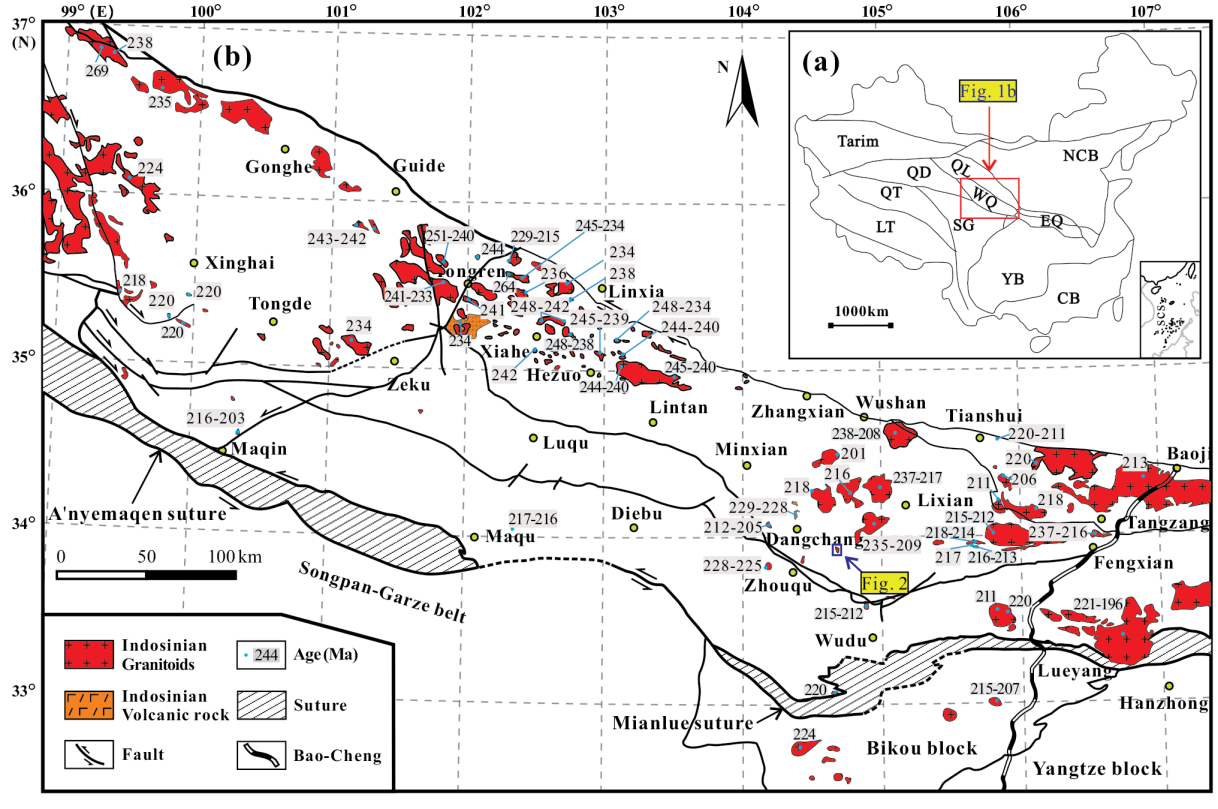

Figure 1. (**a**) Simplified geological map of China, showing the major tectonic units (after Zheng et al. 2010). (**b**) Geological map of the West Qinling Orogenic Belt, showing the distribution of Early Mesozoic granitoids (after Hu et al. 2019; Li et al. 2015; Luo et al. 2012; Xing et al. 2020; Zeng et al. 2018). Data sources for the zircon U-Pb ages are given in Online Materials[1] Table OM1. Place names: WQ = West Qinling; SG = Songpan-Garzê Terrane; QD = Qaidam; QL = Qilian Terrane; NQ = North Qinling; YB = Yangtze Block; NCB = North China Block; SCS = South China Sea; QT = Qiangtang Terrane; LT = Lhasa Terrane; CB = Cathaysia Block. (Color online.)

diorite pluton in the Zhuyuan area, West Qinling, which has complex mineral assemblages and shows remarkably whole-rock high-Sr/Y properties, a diagnostic imprint of adakitic rocks. This makes it a valuable target for exploring the contributions of different generations of minerals to the nature of adakitic granitoids. In this study, we have classified several types of amphiboles, plagioclase, and pyroxenes in the Zhuyuan pluton. Multiple lines of evidence support open-system processes, including pluton construction from multiple generations of antecrysts and magma batches in a felsic magma reservoir at shallow crustal depths. Furthermore, we argue that water-fluxed melting of intermediate to felsic sources controls the development of high-Sr/Y interstitial melts of the studied pluton, and it has no tectonic indication for thickened/delaminated mafic lower curst in spite of emplacement during post-collisional settings.

Sample descriptions

The Zhuyuan pluton investigated in this study intruded Devonian strata (the Wangjiaba, Weijiamu, and Yuchiba Formation) in the eastern part of the West Qinling Orogenic Belt (Figs. 1b and 2). All 17 samples are classified as granodiorites (Online Materials[1] Table OM1) (Streckeisen 1976). They display a medium- to fine-grained texture (Figs. 3a–3b). Rock-forming minerals include quartz (Qtz: ~20 vol%), plagioclase (Pl: 40–45 vol%), K-feldspar (Kfs: 15–20 vol%), biotite (Bt: ~5 vol%), amphibole (Amp: 5–10 vol%), clinopyroxene (Cpx: ~5 vol%), and orthopyroxene (Opx: <2 vol%). Accessory minerals are apatite, zircon, titanite, and magnetite.

Two types of plagioclase crystals are identified. One is clear without resorbed cores or oscillatory zoning; it occurs as phenocrysts or microlites in the groundmass and generally exhibits polysynthetic twinning (Fig. 3b). The other type commonly displays oscillatory zoning with patchy- or sieve-textured cores surrounded by clear rims (Figs. 3c–3d). The sieve texture (Fig. 3c) indicates disequilibrium or resorption and thus implies a xenocrystic (Xu et al. 1999) or antecrystic origin (Jerram and Martin 2008) for the cores. K-feldspar is anhedral and generally measures <1 mm (Fig. 3b).

Pyroxenes display poikilitic textures (Figs. 3e–3i), are anhedral to subhedral, and have sizes of 0.05–1 mm in length. All Cpx and Opx with ragged margins are enclosed by amphibole, reflecting the formation of amphibole at the expense of pyroxene (Figs. 3e–3i). Based on backscattered electron (BSE) images and geochemical characteristics, we identify three types of Cpx: unzoned (Type-1 Cpx), normally zoned (Type-2 Cpx), and reversely zoned (Type-3 Cpx) crystals. In BSE images, both Type-2 and Type-3 Cpx (Fig. 3g) show zoning with core–rim textures, while Opx does not display zoning (Fig. 3i).

Amphibole is one of the principal mineral phases in the Zhuyuan granodiorites that occasionally form aggregates. Amphiboles are euhedral to subhedral, with sizes of 0.01–2.5 mm in diameter, have distinct brown to pale green pleochroism, and do not display zoning in BSE images (Fig. 3g). Some amphiboles display poikilitic textures with biotite (Fig. 3c). According to the texture and particle sizes, we divide them into two types (Type-1 amphibole and Type-2 amphibole). Type-1 amphibole grows along pyroxene grain boundaries and forms a poikilitic texture with pyroxene. Their size is >0.3 mm. Type-2 amphibole does not show poikilitic textures with pyroxene and has smaller grain sizes (0.01–0.4 mm). Most amphiboles occur as corroded grains and do not display equilibrium grain boundary textures where they are in contact with plagioclase and generally exhibit lobate textures (Figs. 3g–3i). This observation suggests that amphibole and plagioclase do not exist in the same equilibrium mineral assemblage. Subhedral to anhedral biotites are khaki to brown, with a length of <1 mm. Biotite usually occurs as interstitial phases associated with K-feldspar and quartz.

Results

Mineral element compositions

Representative in situ major- and trace-element data of Opx, Cpx, Amp, Bt, Pl, and Kfs from the Zhuyuan granodiorites are listed in Online Materials[1] Tables OM3–OM4 and shown in Figures 4 to 6. To ensure the reliability of the data, we only use trace element concentrations higher than 0.1 ppm (generally >5 times the detection limit) for interpretations and calculations. Chemical formulas for biotite and plagioclase were calculated with the AX software (Holland and Blundy 1994). For pyroxene, we use the Geokit software (Lu 2005), and for amphibole, we use the method proposed by Li et al. (2020a).

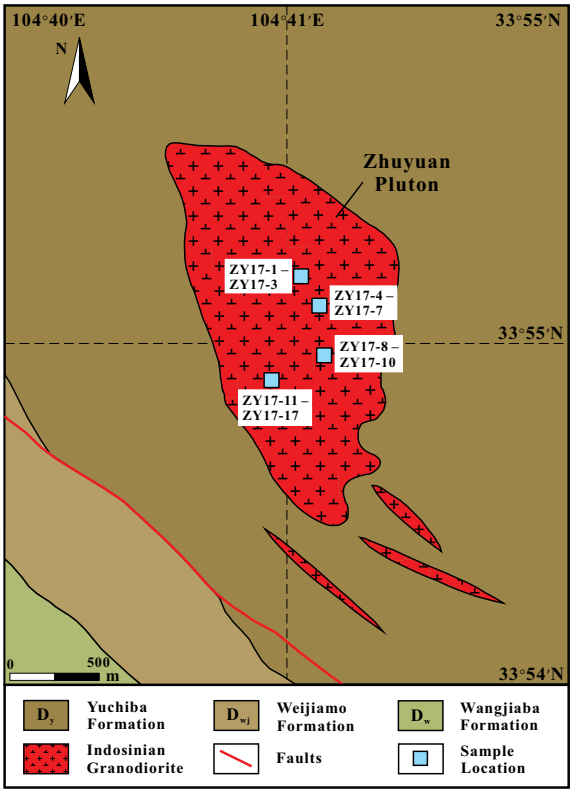

Figure 2. The geological sketch map of the Zhuyuan pluton. (Color online.)

To determine trace-element distributions in mineral phases, several mineral grains were selected for LA-ICP-MS element mapping. A total of 51 elements were mapped for these minerals, and Figures 7–9 display the elements of interest (i.e., Al, Sr, Y, REE, Cr, and Ni) and important parameters (Sr/Y and X_{Mg} values). Figures 7 and 9 present compositional profiles across core-rim interfaces, and Online Materials[1] Tables OM4 contain the corresponding data.

Clinopyroxene. Clinopyroxene shows a large range of SiO_2 (50.0–54.1 wt%) and MgO (12.4–17.1 wt%) contents, high X_{Mg} ($Mg/[Mg+Fe^{2+}] \times 100$) of 70.0–86.9, and variable ΣREEs (37.8–245 ppm), Cr (145–5821 ppm), and Ni (56.2–346 ppm) abundances (Table 1; Online Materials[1] Table OM4). All are classified as diopside or augite (Fig. 4a). Several grains exhibit compositional zonation (Fig. 5). From BSE images and geochemical data, we identify three types of Cpx (Fig. 5): unzoned, normally zoned, and reversely zoned.

Unzoned Cpxs (Type-1 Cpx) are subhedral to anhedral and are diopside and augite (Fig. 4a). We further divide them (Type-1A and Type-1B) based on their FeO^T contents, X_{Mg} values, and chondrite-normalized REE patterns, and both subtypes may occur in a single thin section. Type-1A Cpx is

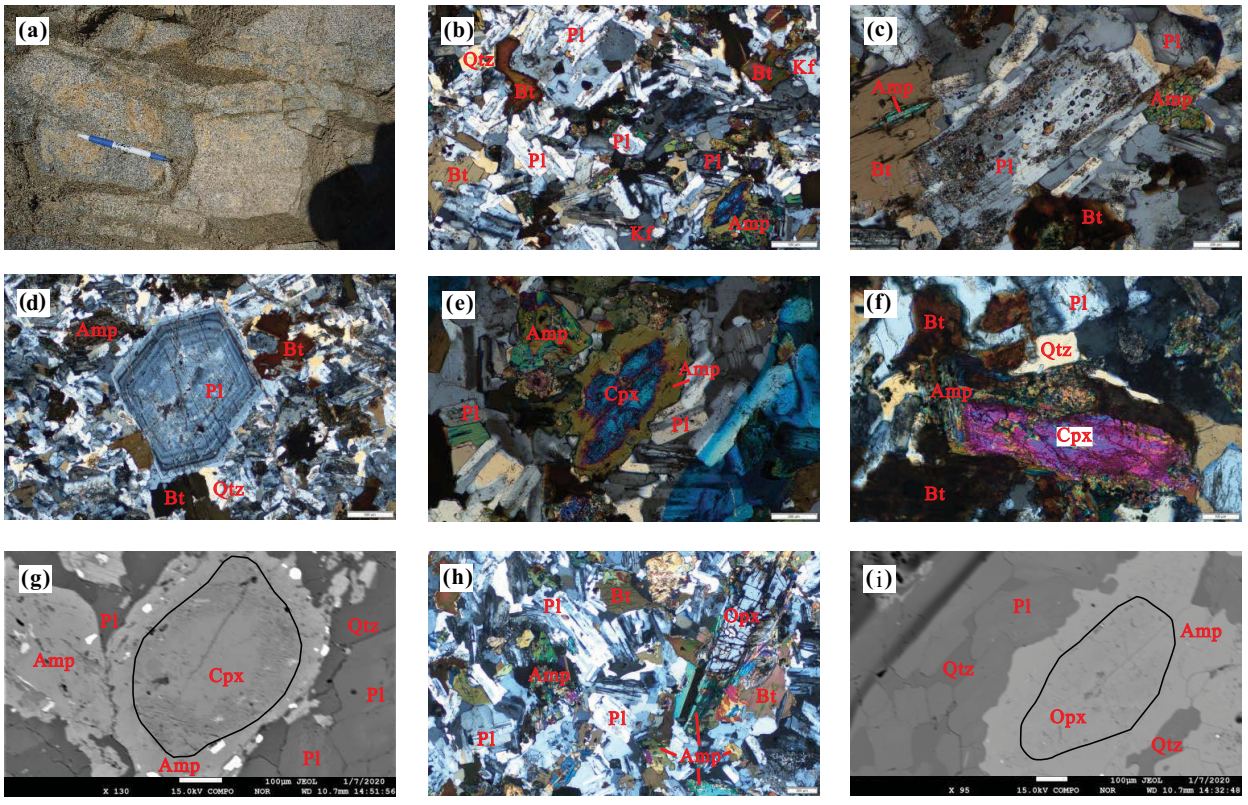

Figure 3. Representative field and microstructural photographs of the Zhuyuan pluton. (**a**) Photograph of the Zhuyuan granodiorites. (**b**) Plagioclases with polysynthetic twinning. (**c**) A plagioclase phenocryst with a sieve texture. (**d**) A plagioclase phenocryst with oscillatory zoning. (**e**) A clinopyroxene crystal enclosed by amphibole. (**f**) A clinopyroxene crystal enclosed by amphibole and biotite. (**g**) A clinopyroxene crystal with clear core–rim texture. (**h**) An orthopyroxene crystal enclosed by amphibole. (**i**) An unzoned orthopyroxene (black outline) mantled by amphibole. Mineral abbreviations: Cpx = clinopyroxene; Opx = orthopyroxene; Amp = amphibole; Bt = biotite; Pl = plagioclase; Kf = K-feldspar; Qtz = quartz. (Color online.)

characterized by high X_{Mg} (72.6–81.7; Fig. 5a), variable FeO^T (6.63–9.69 wt%), and low ΣREEs (54.3–75.0 ppm; Online Materials[1] Tables OM3–OM4). They have chondrite-normalized REE distribution patterns with negative slopes and moderately negative Eu anomalies (Eu/Eu* = 0.54–0.68) (Fig. 6a). The primitive mantle-normalized trace element patterns (Fig. 6b) show depletions in Sr, P, Nb, Ta, Zr, Hf, and Ti, and enrichments in Pr, Nd, and Sm.

Type-1B Cpx has higher FeO^T (9.67–11.0 wt%), Cr (551–1033 ppm), Ni (185–187 ppm), and ΣREEs (135–189 ppm) but slightly lower X_{Mg} (70.0–76.5; Fig. 5b; Table 1) than Type-1A Cpx. In addition, the Type-1B Cpx exhibits moderately negative Eu anomalies (Eu/Eu* = 0.41–0.43, Fig. 6a). The primitive mantle-normalized trace element patterns (Fig. 6b) of both sub-types are similar.

Normally zoned Cpx is subhedral, with slightly darker cores and brighter rims (Figs. 5c–5d). The cores exhibit high X_{Mg} (76.1–80.9; Fig. 5d; Table 1) and Cr contents (1210–1377 ppm) but low ΣREEs (53.7–60.9 ppm). Their chondrite-normalized REEs (Fig. 6c) display weakly negative Eu anomalies (Eu/Eu* = 0.73–0.78). The Type-2 Cpx cores show significant depletions in HFSEs (e.g., Nb, Ta, Zr, Hf, and Ti), K, and P and enrichments in Pb and Nd (Fig. 6d). In comparison with the Type-2 Cpx cores, their rims have slightly higher FeO^T (8.75–9.92 wt%) and ΣREEs (139–245 ppm), but lower MgO (12.4–14.6 wt%) contents and X_{Mg} (71.5–76.2). In addition, the Type-2 Cpx rims have much stronger negative Eu anomalies (Eu/Eu* = 0.32–0.46, Fig. 6c) and larger ranges of Nb, Ta, and K concentrations (Fig. 6d).

Reversely zoned Cpx (Type-3 Cpx) is subhedral with brighter cores and darker rims in BSE images (Figs. 5e–5f). The bright cores contain 14.3–16.0 wt% of MgO with X_{Mg} of 74.3–83.2, are classified as diopside and augite with Wo = 41.8–46.5 mol% (Fig. 4a), have slight negative Eu anomalies (Eu/Eu* = 0.82–0.97; Fig. 6e). As revealed by primitive mantle-normalized trace element patterns, rims of the Type-3 Cpx show depletions in HFSEs (e.g., Nb, Ta, Zr, Hf, and Ti), Ba, K, and P but enrichments in Nd, Th, and Pb (Fig. 6f). By contrast, the dark rims contain slightly more MgO (14.6–17.1 wt%) with X_{Mg} of 75.5–86.9 (Fig. 5f; Table 1), are augite with a lower Wo content (42.1–44.1mol%). The BSE darker rims show similar primitive mantle-normalized trace element patterns as the bright cores (Fig. 6e), but significantly higher Cr (3480–5821 ppm) and Ni (244–346 ppm) contents.

One Type-3 Cpx from sample ZY17–4 was selected for LA-ICP-MS element mapping. The Cr and Ni concentrations

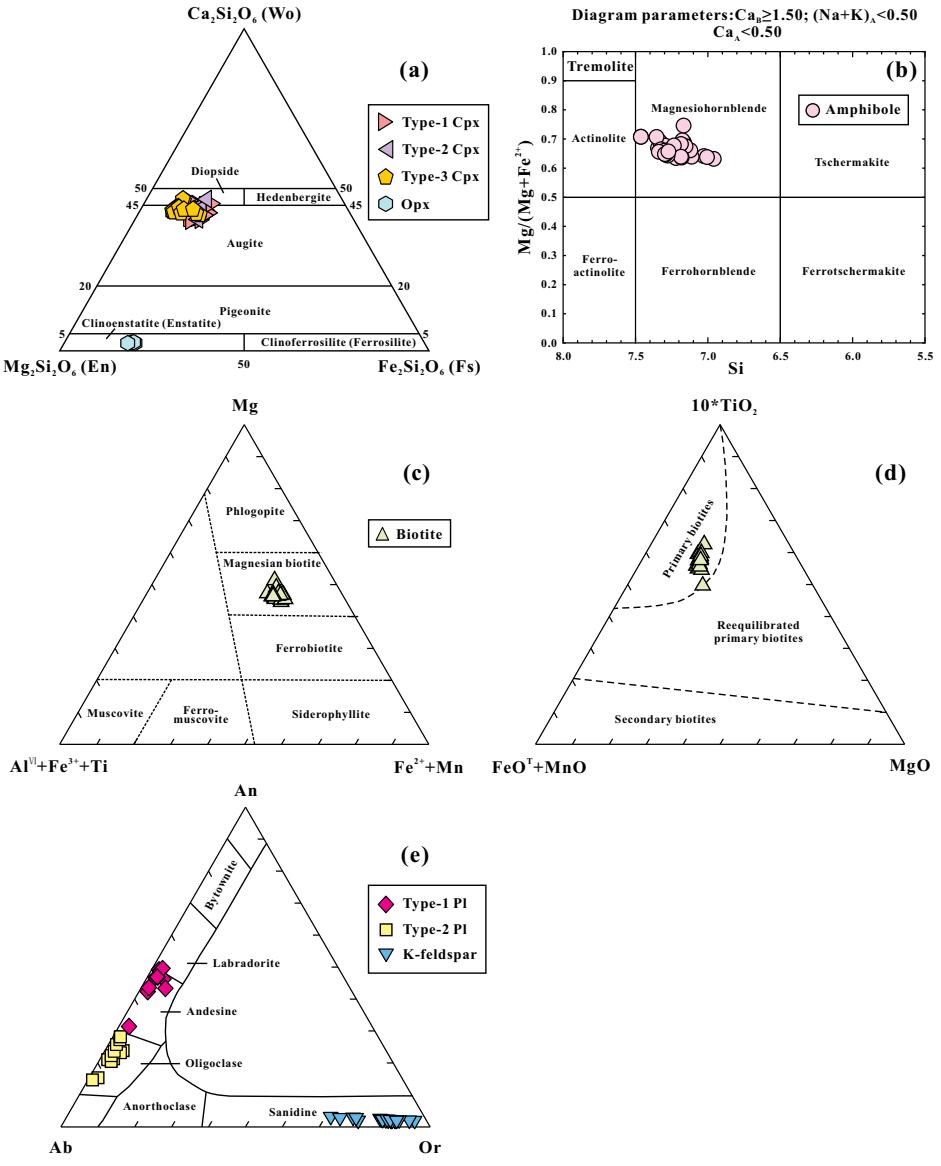

Figure 4. Classification diagrams for rock-forming minerals from the granodiorites of the Zhuyuan pluton. (**a**) Wo-En-Fs ternary diagram for pyroxenes (after Morimoto et al. 1988). (**b**) Mg/(Mg + Fe^{2+}) vs. Si diagram for amphiboles (after Leake et al. 1997). (**c**) Ternary Mg–(Fe^{2+} + Mn)–(Al^{VI} + Fe^{3+} + Ti) (apfu) diagram for biotite (after Foster 1960). (**d**) Ternary 10 × TiO_2–(FeO^T + MnO)–MgO (wt%) diagram for biotite (after Nachit et al. 2005). (**e**) Or-Ab-An ternary diagram for feldspars (after Smith 1974). Abbreviations: Cpx = clinopyroxene; Opx = orthopyroxene; Ab = albite; Or = orthoclase; An = anorthite; Pl = plagioclase; Amp = amphibole; Bt = biotite; Kfs = K-feldspar. (Color online.)

are higher in the rim than in the core (Fig. 7), likely reflecting a mafic magma recharge event. Element data of the corresponding cross section (Profile A) are provided in Online Materials[1] Table OM4. The Cr contents are lower in the core (530–1500 ppm), but higher in the rim (2315–10375 ppm), which also applies to Th and Sr, resulting in higher Sr/Y values in the rim (core: 4.45–9.49, rim: 5.85–18.5; Online Materials[1] Table OM4).

Orthopyroxene. Orthopyroxene is classified as enstatite (Fig. 4a) with a compositional range of $Wo_{2.02–2.58}En_{78.9–80.9}Fs_{17.1–19.0}$. They have high Cr (1854–2261 ppm) and Ni (591–837 ppm) concentrations, high X_{Mg} of 80.9–82.8, and low abundances of Al_2O_3 (1.76–2.86 wt%), TiO_2 (0.09–0.18 wt%), and CaO (1.01–1.30 wt%; Xie et al. 2023), and very low ΣREEs (0.73–2.82 ppm; Online Materials[1] Table OM4).

On a LA-ICP-MS element map of one representative Opx of sample ZY17–15 (Fig. 8), the crystal shows a ubiquitous enrichment of Cr and Ni. Notably, the Sr/Y values increase significantly along the cleavage, cracks, and edges of this crystal, probably reflecting the influence of late-stage magmatic/hydrothermal activity.

Amphibole. Using the amphibole nomenclature and classification schemes of Leake et al. (1997) and Li et al. (2020a), all the analyzed amphiboles are calcic (Ca_B ≥1.5 apfu, $(Na+K)_A$ <0.5 apfu) and are classified as magnesiohornblende (Fig. 4b). There are no obvious compositional differences between larger (Type-1 amphibole) and smaller (Type-2 amphibole) amphiboles (Online Materials[1] Table OM3–OM4). They feature variable SiO_2 (46.5–51.0 wt%), Cr (77–1038 ppm), and Ni (103–205 ppm) contents, moderately high X_{Mg} (63.1–74.6), and limited ranges in Al_2O_3 (4.22–6.14 wt%), TiO_2 (0.48–1.21 wt%), and total alkalis (Na_2O + K_2O: 1.11–1.79 wt%). The amphiboles show high ΣREEs (303–712 ppm), pronounced negative Eu anomalies (Eu/Eu* = 0.14–0.29), and obvious depletion of

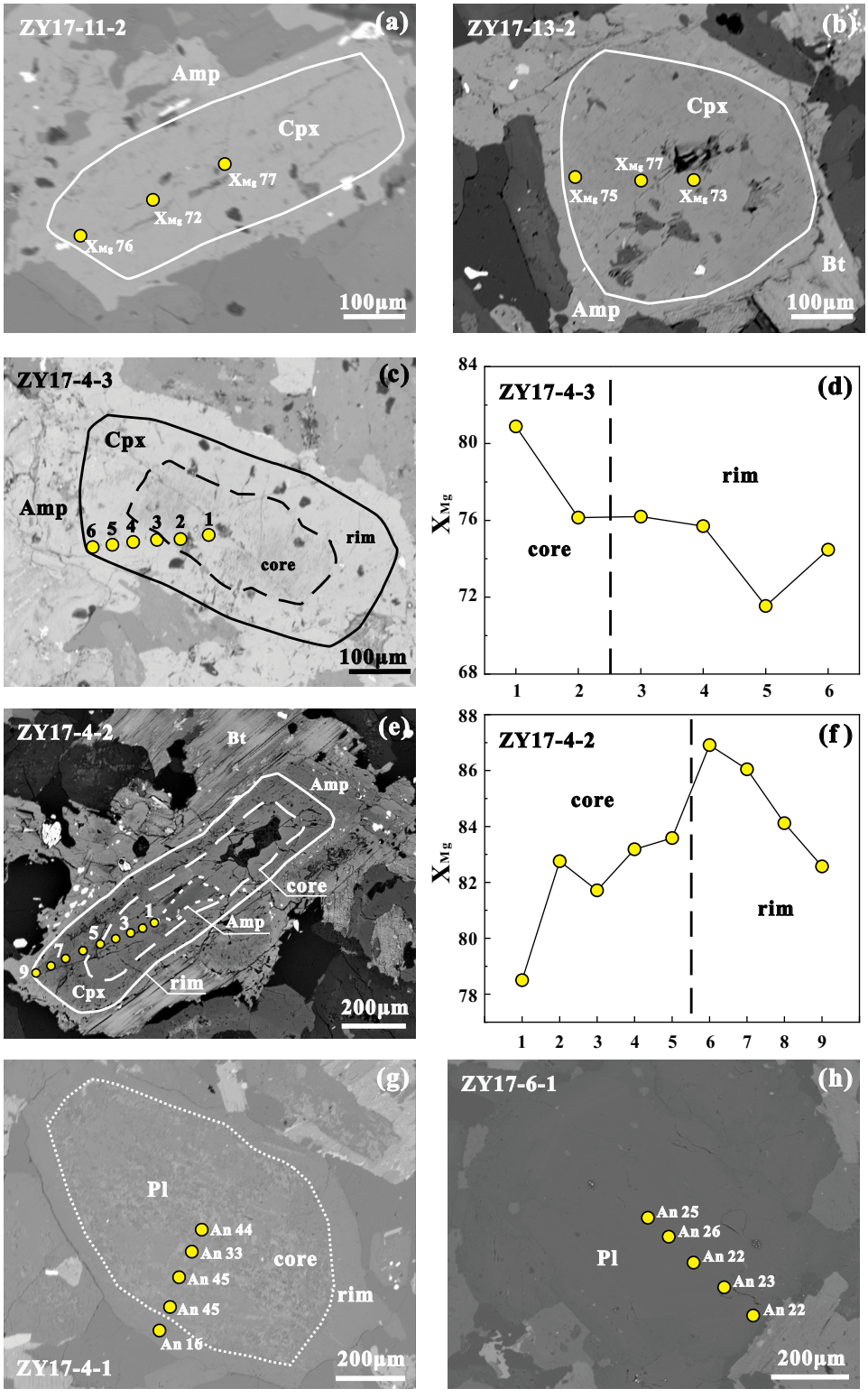

Figure 5. Backscattered electron images and X_{Mg} and An contents for selected clinopyroxenes and plagioclases, respectively. (**a** and **b**) Optically unzoned clinopyroxenes (ZY17-11-2 and ZY17-13-2). (**c**) and (**d**) A normally zoned clinopyroxene and the core–rim profile of its X_{Mg} (ZY17-4-3). (**e** and **f**) A reversely zoned clinopyroxene and the core–rim profile of its X_{Mg} (ZY17-4-2). (**g**) A plagioclase crystal with a sieve texture (ZY17-4-1). (**h**) A plagioclase crystal without sieve texture (ZY17-6-1). Mineral abbreviations: Cpx = clinopyroxene; Opx = orthopyroxene; Pl = plagioclase; Amp = amphibole; Bt = biotite. (Color online.)

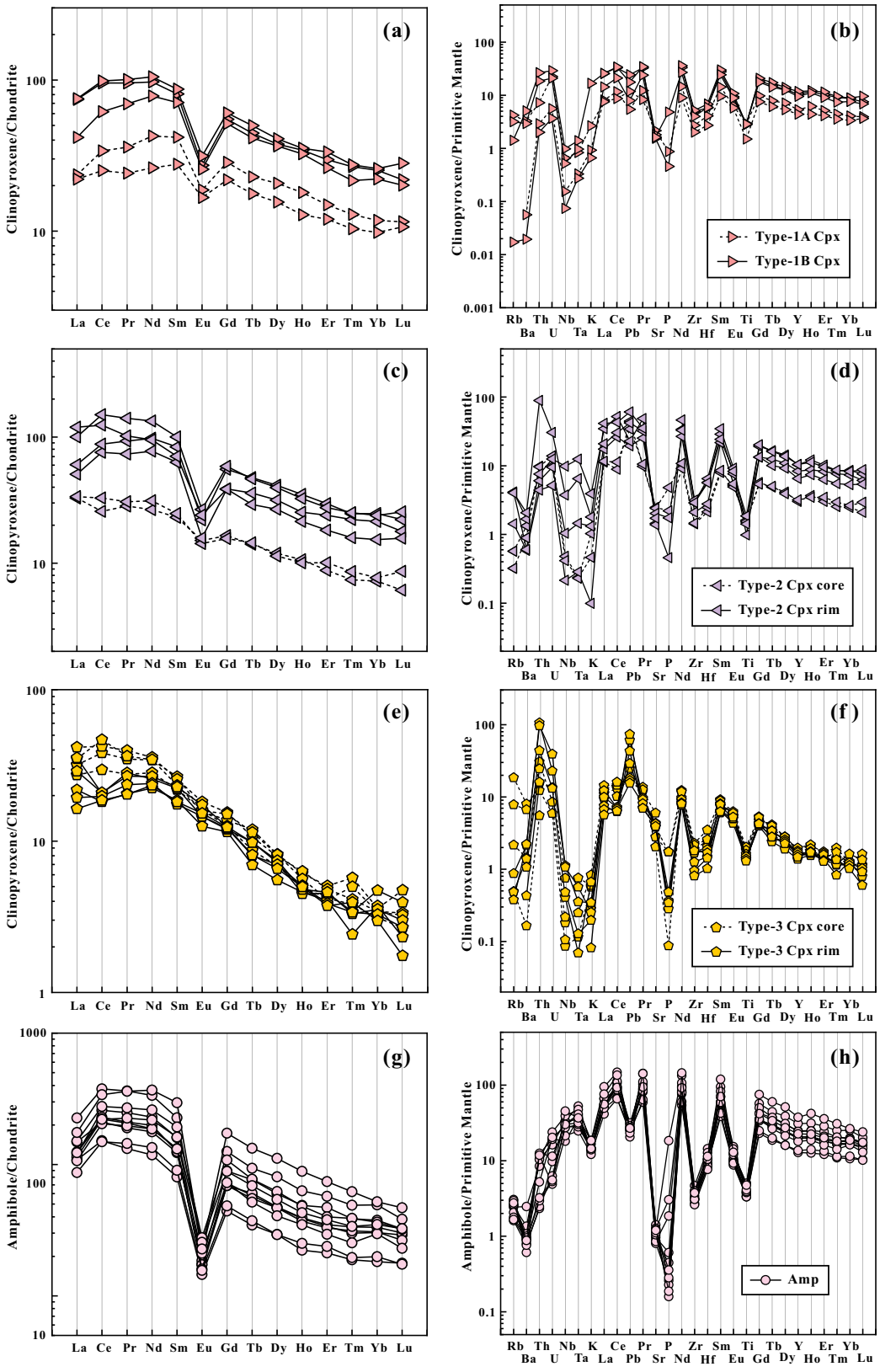

Figure 6. (**a**, **c**, **e**, and **g**) Chondrite-normalized REE patterns and (**b**, **d**, **f**, and **h**) primitive mantle-normalized trace element patterns for clinopyroxene and amphibole from the Zhuyuan pluton. The normalization values are from Sun and McDonough (1989). (Color online.)

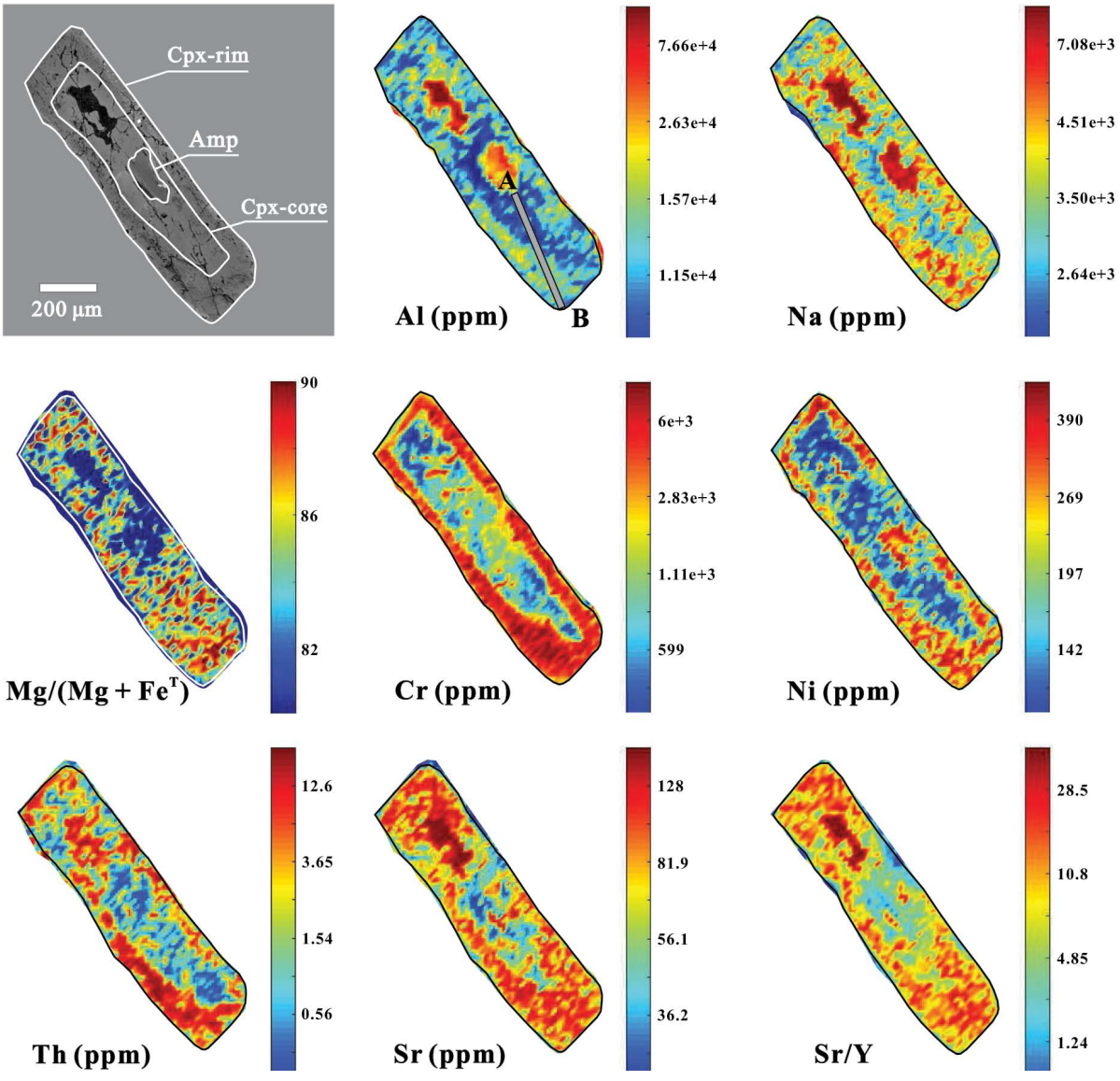

Figure 7. Back scattered electron image and LA-ICP-MS maps of representative elements and important parameters for a reversely zoned clinopyroxene from sample ZY17–4. All LA-ICP-MS maps show probability density abundances to accentuate distribution characteristics. LA-ICP-MS data of Profile A extracted parallel to line A–B are listed in Online Materials[1] Table OM4. (Color online.)

HREE relative to LREE (Fig. 6g). They are depleted in Ba, Sr, and Zr, but enriched in Nd and Sm (Fig. 6h).

LA-ICP-MS element mapping of one magnesiohornblende (Type-2 amphibole) abutting Opx (Fig. 8) confirms the compositional features (e.g., relatively high X_{Mg} and low Sr/Y) of the single spot in situ analysis.

Biotite. Biotite exhibits relatively consistent Al^{IV} values (1.13 to 1.32 apfu) and contains high FeO^T (19.1–20.6 wt%) and Al_2O_3 (12.7–14.6 wt%) and moderate MgO (11.1–14.3 wt%); X_{Mg} are 54.4–61.5 (Table 1). According to the classification of Foster (1960), the biotites are within the compositional range of magnesian biotite (Fig. 4c). Nachit et al. (2005) discriminate magmatic or primary biotite from secondary or re-equilibrated primary biotite in a 10 × TiO_2–FeO*(= FeO + MnO)–MgO ternary diagram (Fig. 4d). On this diagram, all analyzed biotites plot in the primary biotite field. The trace element compositions of the biotites vary slightly (Online Materials[1] Table OM4): they have low abundances of Sr (1.74–6.74 ppm), relatively low concentrations of Y (0.15–0.33 ppm), with high values of Sr/Y (17.5–43.8), relatively low ΣREEs (ranging from 0.30 to 4.12 ppm), relatively high contents of Rb (317–601 ppm), Ba (471–6055 ppm), Nb (27.5–53.7 ppm), and Ni (191–283 ppm), but low abundances of Ta (1.00–4.79 ppm) and Hf (0.12–0.28 ppm).

One biotite from sample ZY17–4 was selected for LA-ICP-MS element mapping (Fig. 9) and acquisition of one cross section (Profile B; Online Materials[1] Table OM4). The core of this biotite features lower Sr, Cu, and Pb concentrations than

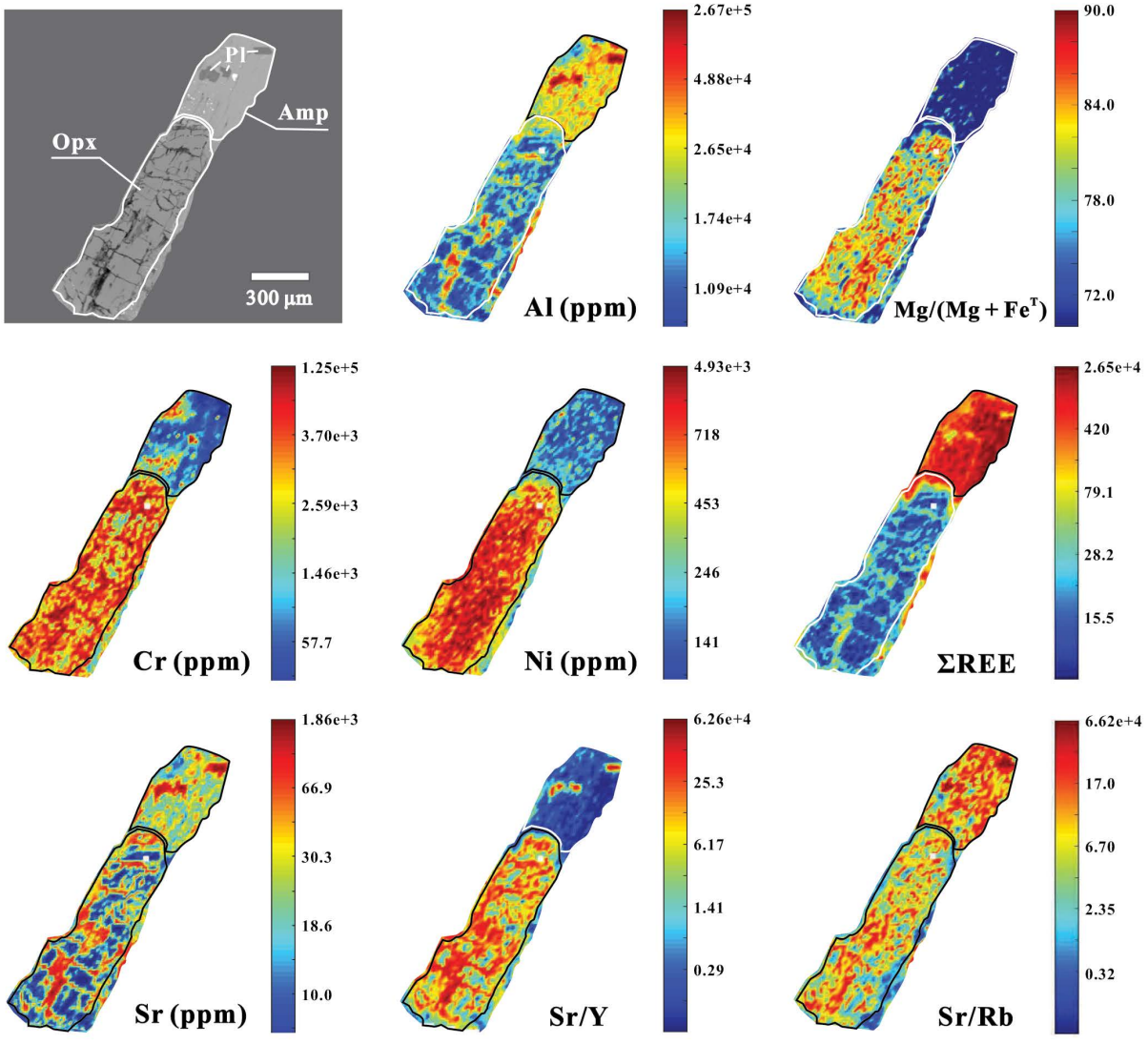

Figure 8. Back scattered electron image and LA-ICP-MS maps of representative elements and important parameters for an orthopyroxene + amphibole assemblage from sample ZY17–15. All LA-ICP-MS maps show probability density abundances to accentuate distribution characteristics. (Color online.)

the rim. The entire biotite shows high-Sr/Y values (7.32–174), relatively high-X_{Mg} values (52.1–60.1), and high abundances of Ni (307–459 ppm), Ba (2840–6438 ppm), and Rb (191–382 ppm). All these characteristics are similar to those of the biotites described above based on single spot in situ analysis.

Plagioclase is mainly classified as oligoclase–andesine and subordinately as labradorite (Fig. 4e), with anorthite contents (An) of 14.9–51.6 mol% (Table 1; Online Materials[1] Tables OM3–OM4). We identify two distinct plagioclase populations: sieve-textured plagioclase cores (Type-1 Pl) with rim overgrowths (Fig. 5g), and unreacted plagioclases devoid of sieve textures (Type-2 Pl, Fig. 5h). The sieve-textured plagioclase cores (Type-1 Pl) exhibit higher An (32.9–51.6 mol%) and Rb contents (10.4–318 ppm) than their overgrowth rims (Type-2 Pl; 15.6–29.4 mol% and 0.92 ppm, respectively; Table 1). Type-2 plagioclases are homogeneous in composition and contain low An (14.9–26.9 mol%) and Rb (0.31–4.28 ppm; Table 1). Since the composition of the sieve-textured plagioclase rims is similar to that of the Type-2 plagioclase, they possibly grew at the same time. In other words, we may consider the rims on Type-1 grains as part of the same geochemical group (Type-2 plagioclase). Both types of plagioclases have variable ΣREEs abundances (12.8–45.3 ppm), high Sr (865–1519) ppm but extremely low-Y contents (0.10–0.22 ppm), and high Sr/Y (4254–14513) (Table 1).

LA-ICP-MS element mapping of several plagioclase inclusions within the amphibole featured in Figure 8 shows that plagioclases have high-Sr contents (~66.9–1860 ppm) and high Sr/Y (~25.3 to 62600) and Sr/Rb (~17.0 to 66200) values, similar to Type-2 plagioclases and sieve-textured plagioclase rims described above. This indicates that the appearance of these plagioclases included by amphibole might be the result of the

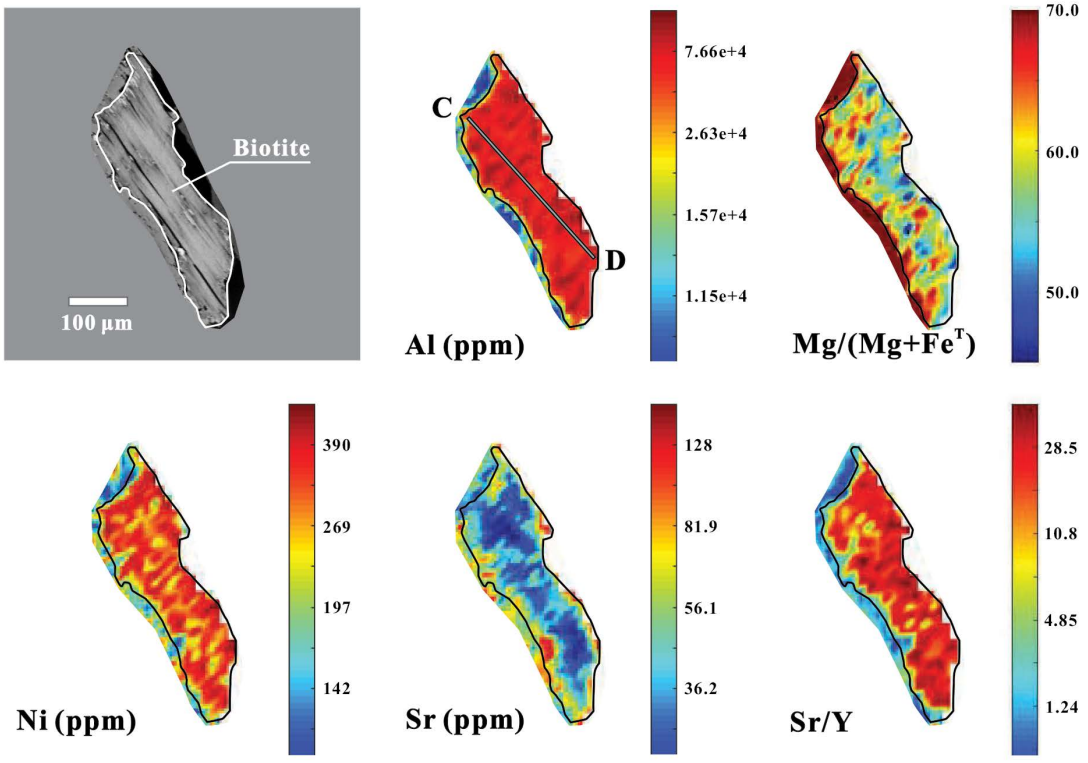

Figure 9. Back scattered electron image and LA-ICP-MS maps of representative elements and important parameters for a biotite from sample ZY17–4. All LA-ICP-MS maps show probability density abundances to accentuate distribution characteristics. LA-ICP-MS data of Profile B extracted parallel to line C–D are listed in Online Materials[1] Table OM4. (Color online.)

sectioning-effect (plagioclases protruding into amphibole from the top or bottom of the thin section), and these plagioclases do not crystallize earlier than hornblende. The similar sectioning-effect also occurs between amphibole and pyroxene (Fig. 7).

It should be noted that HREE are sometimes close to or below the detection limits in plagioclase, and the extremely high-Sr/Y values of some plagioclase crystals are not accurate.

K-feldspars. K-feldspars are sanidine, and their orthoclase (Or) contents range from 72.4 to 95.8 mol% (Online Materials[1] Table OM3). They display very high positive Eu anomalies (Eu/Eu* >4.01, Tables 1; Online Materials[1] Table OM4), high concentrations of Rb (197–338 ppm), Ba (1077–5925 ppm), and Sr (535–1029 ppm), low contents of Y (≤0.1 ppm, the Y contents of several crystals are below the detection limit), with correspondingly extremely high-Sr/Y values (>5345; Table 1).

Crystal size distribution (CSD)

We analyzed a 354 mm^2 area across two thin sections and observed 2246 amphiboles with non-poikilitic textures covering an area of 41.4 mm^2 (see Online Materials[1] Table OM5 for CSD analysis data of these amphiboles). The crystal sizes range from 0.01 to 0.4 mm (Figs. 10a–10b). On a plot of the logarithm of the crystal population density [ln(n)] vs. size (L) (Figs. 10c–10d), the CSDs of both samples exhibit a significant change in slope from a shallow gradient in the larger crystals to a steeper gradient in the smaller crystals. As shown in Figure 10, the amphibole CSD may be separated into at least two groups, and the regression curve equations of different groups of amphibole CSDs are given in the figure. Linear CSD curves generally indicate that the crystal population densities are primarily controlled by crystal nucleation and growth, whereas kinked CSDs are usually

Table 1. The important parameters of rock-forming minerals of the Zhuyuan granodiorites

Mineral	X_{Mg}	An/Or	Sr (ppm)	Y (ppm)	Rb (ppm)	Sr/Y	ΣREE (ppm)	Texture	Type
Type-1A Cpx	72.6–81.7	–	34.4–45.5	20.1–24.4	2.69	1.41–2.26	54.3–75.0	poikilitic texture, non-zoned	antecrysts
Type-1B Cpx	70.0–76.5	–	32.8–38.2	43.3–53.3	0.90–2.03	0.61–0.80	135–189		antecrysts
Type-2 Cpx core	76.1–80.9	–	50.9–52.2	13.8–14.5	0.20–0.36	3.51–3.79	53.7–60.9	poikilitic texture, normally zoned	antecrysts
Type-2 Cpx rim	71.5–76.2	–	29.3–42.7	29.7–47.7	0.91–2.62	0.61–1.22	139–245		antecrysts
Type-3 Cpx core	74.3–83.2	–	43.1–127	7.57–8.96	0.31–11.7	5.30–14.8	51.0–68.6	poikilitic texture, reversely zoned	antecrysts
Type-3 Cpx rim	75.5–86.9	–	82.5–91.9	6.27–7.57	0.24–0.55	11.7–13.2	37.8–46.6		antecrysts
Orthopyroxene	80.9–82.8	–	0.29–0.84	1.29–3.77	0.10–0.22	0.45–0.65	0.72–2.82	poikilitic texture	antecrysts
Amphibole	63.1–74.6	–	17.0–29.8	58.2–141	1.54–1.94	0.15–0.33	303–693	disequilibrium boundary texture	antecrysts
Type-1 Pl	–	An: 32.9–51.6	965–1519	0.14–0.21	10.4–318	6002–9768	12.8–45.3	sieve texture	antecrysts
Type-2 Pl	–	An: 14.9–29.4	865–1494	0.10–0.22	0.31–4.28	4254–14513	15.3–36.2	non-sieve texture	orthocrysts
Biotite	54.4–61.5	–	1.74–6.74	0.15–0.33	317–601	17.5–43.8	0.30–4.12	interstitial mineral	orthocrysts
K-feldspar	–	Or: 72.4–95.8	535–1029	<0.1	197–338	>5345	1.47–16.1	interstitial mineral	orthocrysts

explained by the mixing of different crystal generations (Burney et al. 2020; Higgins 1996; Morgan et al. 2007; Wang et al. 2019; Yang et al. 2010).

Discussion

A key problem in interpreting adakitic rocks in continental settings is that felsic magmatic rocks commonly represent an assembly of interstitial melts and several crystal populations with different origins (Namur et al. 2020 and references therein). In the case of the Zhuyuan granodiorites, we also hypothesize that their high-Sr/Y signal could be derived from multiple batches of magmas within an open magmatic system. We combine whole-rock geochemical characteristics with in situ mineral compositions to highlight the potential role of magma mixing in the formation of the Zhuyuan granodiorites. The relevant discussion is provided in the Online Materials[1]. Furthermore, in subsequent discussions, we focus on the origin and evolutionary process of the high-Sr/Y signature of the Zhuyuan granodiorites.

Crystal-melt equilibria

Assuming that the minerals were in equilibrium with the corresponding host melts during crystallization, the geochemical compositions of the parental magmas may be estimated with compositionally appropriate mineral-melt partition coefficients (K_D; Online Materials[1] Table OM6). Based on petrographic observations (Fig. 3), we have determined the complex mineral associations of the Zhuyuan granodiorites, which are mainly composed of 11 kinds of minerals, including three types of Cpxs, Opx, two types of amphiboles, two types of plagioclases, Bt, Kfs, and Qtz. Because there is no difference in compositional characteristics and crystallization conditions between the Type 1 amphibole and Type-2 amphibole (Online Materials[1] Tables OM3–OM4), we consider them to have formed in the same *trans*-crustal magmatic system. In addition, Bt, Kfs, and Qtz are the interstitial minerals, and are the most easily identifiable late-stage crystalline mineral phases, which could have possibly formed in the same magmatic environment. Thus, we provisionally define eight magma environments (A, B, C, D, E, F, G, and H) in which different types of minerals crystallized (Table 2). Based on the mineralogical characteristics, we initially classified the magmatic environments into four subtypes: A-D, E, F-G, and H. In the following, these magma environments could be identical, similar, or distinct. We will further discuss the significance of these below in the "Crystal cargoes in the magmatic plumbing system" section.

Environments A, B, C, and D: The parental magmas in which the various types of pyroxenes crystallized. We use the Fe–Mg exchange coefficient [$K_D(Fe–Mg)^{Cpx–liq}$] value of 0.27 ± 0.03 to calculate the Mg# of melts in equilibrium with Cpxs (Pichavant and Macdonald 2007; Putirka 2008; Sisson and Grove 1993). Considering the high X_{Mg} of pyroxenes in this study, we use partition coefficients between pyroxene and basaltic melts to

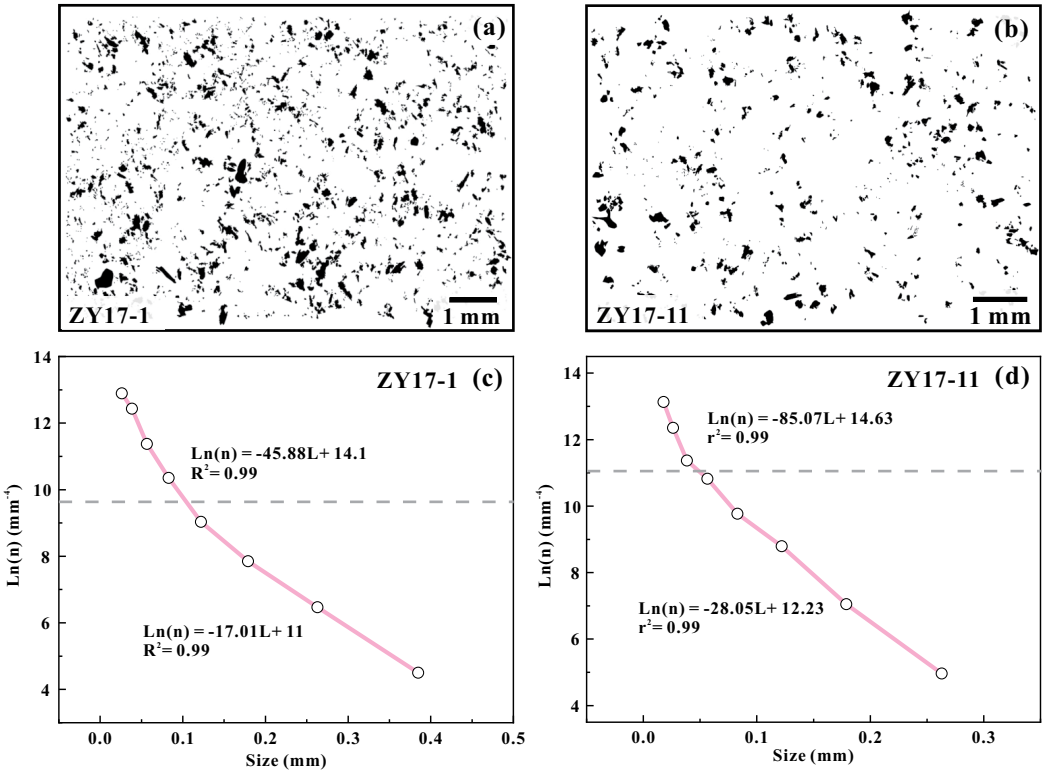

Figure 10. (**a** and **b**) Amphiboles outlined in photomicrographs of samples ZY17–1 and ZY17–11, respectively. (**c** and **d**) The CSD diagrams of ln(*n*) vs. size of amphibole for samples ZY17–1and ZY17–11, respectively, where "*n*" represents the number of grains. Slope and intercept definitions are as follows: Slope = –1/Gt; Intercept = I/G, where nucleation rates (I) and crystal residence reservoir (t) were calculated by assuming a constant crystal growth rate (G; Marsh 1988). (Color online.)

calculate trace-element compositions of the melt in equilibrium with the pyroxene (Bédard 2001; Elkins et al. 2008). Calculated trace-element concentrations of melts in equilibrium with pyroxenes are listed in Table 2 and Online Materials[1] Table OM6.

The calculated equilibrium melts (Environment A) of the Type-1 Cpx have a wide range of Mg# (39.5–55.5) and values of Type-1A (39.5–47.7) and Type-1B Cpx (42.7–55.5) overlap. Melts in equilibrium with Type-1A Cpx exhibit moderately negative Eu anomalies (Eu/Eu* = 0.54–0.68; Fig. 11a), relatively high-Ce/Pb values (83.6 on average), and low Sr/Y values (4.52–7.27) (Fig. 12). Type-1B Cpx equilibrium melts have more pronounced negative Eu anomalies (Eu/Eu* = 0.41–0.43), comparable Ce/Pb values (78.8–156), and lower Sr/Y values (1.97–2.57). Type-1A and Type-1B Cpx equilibrium melts show similar chondrite-normalized rare earth element distribution patterns.

The melts (Environment B) in equilibrium with Type-2 Cpx have Mg# of 41.3 to 54.2. The melts in equilibrium with Type-2 Cpx cores display slight to moderate Eu anomalies (Eu/Eu* = 0.72–0.77; Fig. 11b) and low Sr/Y (11.3–12.2) but high-Ce/Pb values (15.5 on average). Compared with the cores, the melts in equilibrium with Type-2 Cpx rims exhibit more significant negative Eu anomalies (Eu/Eu* = 0.32–0.46), higher ΣREE contents and Ce/Pb values (41.2–133), but lower values of Sr/Y (1.97–3.93).

The melts (Environment C) in equilibrium with Type-3 Cpx span a large range of Mg#. The melts in equilibrium with Type-3 Cpx core have Mg# of 44.7–58.1, high Ce/Pb (23.9–55.7) and Sr/Y (17.0–47.6) values, and slight to negligible negative Eu anomalies (Eu/Eu* = 0.82–0.96; Fig. 11c). Compared with the cores, the melts in equilibrium with Type-3 Cpx rim have on average higher Mg# (48.4–65.0), high Sr/Y (37.6–42.4, Fig. 12a) and Ce/Pb values (12.1 on average, Fig. 12b), and negative Eu anomalies (Eu/Eu* = 0.85–1.02). The melts (Environment D) in equilibrium with Opx have high Mg# of 56.8–59.9 (K_d = 0.31; Price et al. 2012), high mean Ce/Pb values of 11.4 (Fig. 12b), but moderate Sr/Y values (11.7–21.8).

Environment E: The parental magmas in which two types of amphiboles crystallized. Amphibole–liquid partition coefficients for trace elements were calculated using the mineral composition model proposed by Humphreys et al. (2019) and Shimizu et al. (2017). The melts in equilibrium with amphibole (Table 2; Online Materials[1] Table OM6) feature low Mg# (21.7–34.6), negative Eu anomalies (Eu/Eu* = 0.13–0.29; Fig. 11d), and relatively low Sr/Y (4.13–21.6), and medium Ce/Pb values (8.92 on average).

Environments F and G: The parental magmas in which both sieve-textured and clear plagioclase crystallized. The partition coefficients of Sr between plagioclase and silicate melts depend on the chemical composition of plagioclase (Bindeman et al. 1998). Plagioclase-silicate melt partition coefficients for Sr, Rb, and REE were calculated using the mineral composition model of Sun et al. (2017). Partition coefficients for Y and Ba are from Nash and Crecraft (1985). The melts (Environment F) in equilibrium with Type-1 plagioclase have relatively high Sr/Y (218–315) and Sr/Ba values (0.4–1.27), low Sr/Rb (0.2–6.81) and Ce/Pb (3.18–5.59), and positive Eu anomalies (Eu/Eu* = 5.44–8.16; Table 2). By contrast, the melts in equilibrium with Type-2 plagioclase (Environment G) display lower Ce/Pb (1.55–2.27), higher Sr/Rb (26.4–252) and Sr/Ba values (0.99–1.67), the same high-Sr/Y values (96.5–375), and more obvious positive Eu anomalies (Eu/Eu* = 4.85–25.4).

Environment H: The parental magmas in which Bt, Kfs, and Qtz crystallized. Biotite and K-feldspar mainly appear as interstitial minerals, which are the products of late-stage melt. Therefore, we select the partition coefficients of trace elements for melts in equilibrium with biotite and K-feldspar (Nash and Crecraft 1985; Sun et al. 2017; Schnetzler and Philpotts 1970; Ewart and Griffin 1994). The Y contents in the analyzed K-feldspar samples are all lower than 0.1 ppm. Here, we assume 0.1 ppm Y to calculate the Y content of equilibrium melt. The actual content will be much lower than the calculated value, but this does not affect the subsequent discussion. The melts in equilibrium with biotite have high Sr/Y (49.5–124) but low Ce/Pb values (0.01–0.07; Table 2). The melts in equilibrium with K-feldspar are characterized by high-Sr/Y values (> >29), low Ce/Pb values (0.05–0.84), and variable Eu contents (0.35–1.47 ppm; Table 2).

Crystallization conditions

The temperature and pressure of the magma reservoir are essential for our understanding of the origin of different minerals (Blundy and Cashman 2008). Experimental petrology studies have shown that the Cpx and amphibole are sensitive to temperature and pressure during crystallization. Thus, thermobarometers based on compositions of Cpx or amphibole are commonly used to estimate the physical conditions of magma reservoirs (e.g., Higgins et al. 2022; Neave et al. 2019; Neave and Putirka 2017; Putirka 2016; Putirka 2008). We chose the thermometer (Eq. 32d in Putirka 2008) and the barometer (Eq. 32a in Putirka 2008) based on Cpx compositions only to estimate the crystallization temperatures and pressures. The thermobarometer we

Table 2. The important parameters of the melts in equilibrium with rock-forming minerals from the Zhuyuan granodiorites

Equilibrium melt	Mg#	Cr (ppm)	Ni (ppm)	Eu/Eu*	Sr/Y	Sr/Rb	Sr/Ba	Ce/Pb	Environment
Type-1A Cpx	39.5–47.7	46.5–71.2	28.1–46.0	0.54–0.68	4.52–7.27	–	–	42.5–125	A
Type-1B Cpx	42.7–55.5	145–272	92.4–93.5	0.41–0.43	1.97–2.57	–	–	78.8–156	
Type-2 Cpx core	47.2–54.2	318–362	31.9–33.3	0.72–0.77	11.3–12.2	–	–	11.6–19.4	B
Type-2 Cpx rim	41.3–47.3	101–460	34.6–67.7	0.32–0.46	1.97–3.93	–	–	41.2–133	
Type-3 Cpx core	44.7–58.1	38.2–244	45.8–85.1	0.82–0.96	17.0–47.6	–	–	23.9–55.7	C
Type-3 Cpx rim	48.4–65.0	916–1532	122–173	0.85–1.02	37.6–42.4	–	–	5.07–25.5	
Orthopyroxene	56.8–59.9	976–1190	169–239	–	11.7–21.8	–	–	~11.4	D
Amphibole	21.7–34.6	–	–	0.13–0.29	4.13–21.6	–	–	4.4–18.9	E
Type-1 Pl	–	–	–	15.9–23.3	218–315	0.20–6.81	0.40–1.27	3.18–5.59	F
Type-2 Pl	–	–	–	14.6–67.4	96.5–376	26.4–252	0.99–1.67	1.55–2.27	G
Biotite	–	–	–	–	49.5–124	–	–	0.01–0.07	H
K-feldspar	–	–	–	–	> >29	–	–	0.05–0.84	

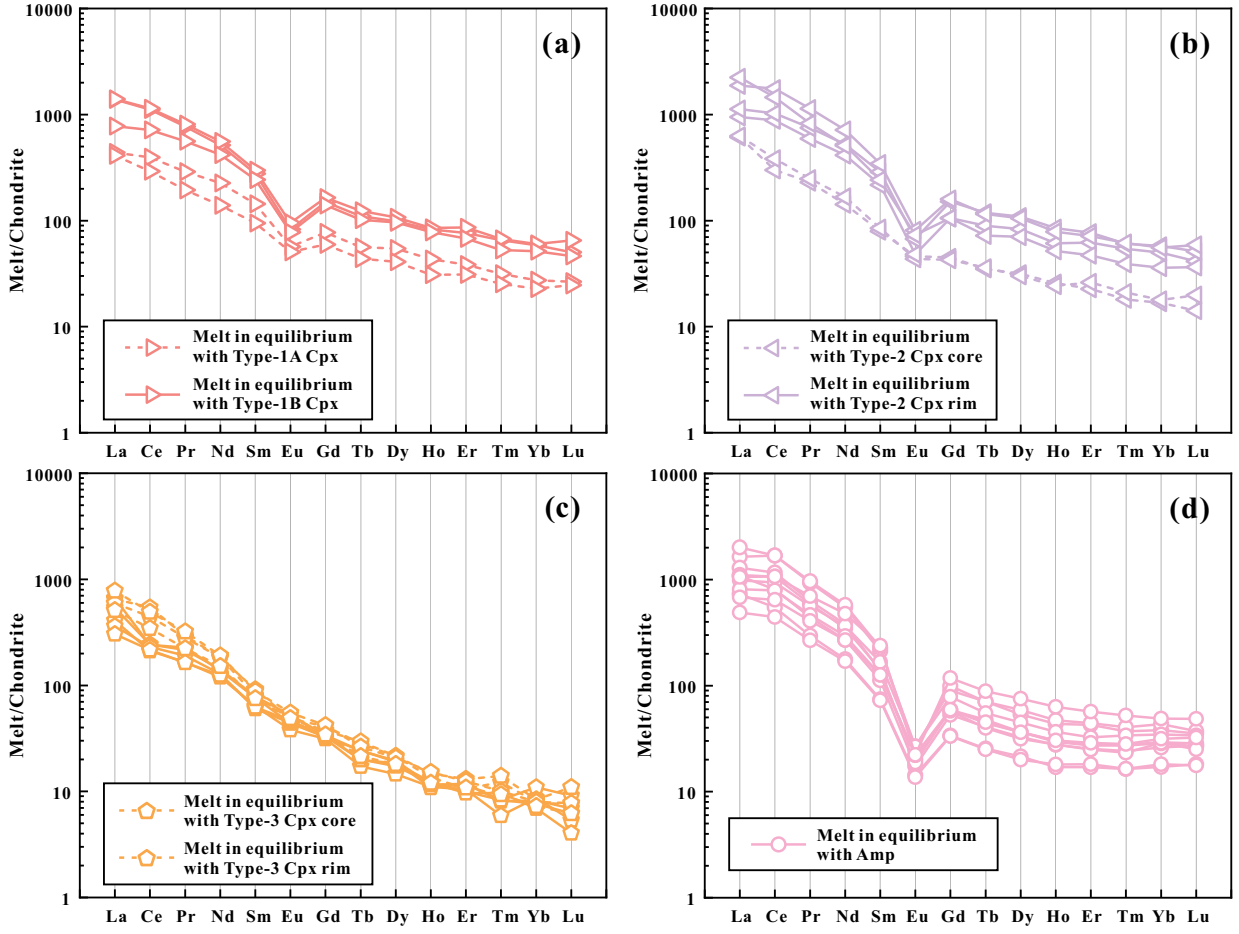

Figure 11. Chondrite-normalized REE distribution patterns for the melts in equilibrium with (**a**) unzoned clinopyroxenes (Type-1 Cpx); (**b**) normally zoned clinopyroxenes (Type-2 Cpx); (**c**) reversely zoned clinopyroxenes (Type-3 Cpx); and (**d**) amphiboles (Amp). The normalization values are from Sun and McDonough (1989). (Color online.)

used produces one standard error of estimate (1se) of ± 58 °C and ± 0.31 GPa, respectively (Putirka 2008). Due to the poikilitic textures and the irregular corrosion boundary between pyroxene and amphibole, the thermochemical reactions at/near the pyroxene-amphibole boundary are significant. It may lead to a large error in conditions with the pyroxene compositions close to the reaction boundary, so we only selected the spot analyses away from the boundary for the corresponding calculation (Table 3).

The estimate temperature based on Type-1, Type-2, and Type-3 Cpx range from 1150 to 1191 °C, 1130 to 1192 °C, and 1173 to 1211 °C, respectively. Estimated pressures vary from 0.48 to 0.75 GPa, 0.4 to 0.84 GPa, and 0.38 to 0.61 GPa, respectively. These values correspond to crystallization depths of 18.1–28.4 km, 15.3–31.7 km, and 14.2–23.0 km, respectively, indicating that Type-1 and Type-2 Cpx crystallized in magma reservoirs at approximately similar depths, while the Type-3 Cpx formed at shallower crustal levels.

In addition, we use the single-phase amphibole thermobarometer in Higgins et al. (2022) to determine the crystallization conditions of both types of amphiboles, which is calibrated using random forest machine learning. The random forest machine learning algorithm can recover subtle nonlinear relationships between phase compositions, pressure, and temperature (Higgins et al. 2022). Therefore, this approach is superior for retrieving the physical conditions of amphibole formation in open magmatic systems. The temperatures calculated from amphibole compositions of the Zhuyuan granodiorites range from 744 ± 38 °C to 814 ± 54 °C. The pressure of amphibole crystallization varies from 0.2 ± 0.02 GPa to 0.35 ± 0.18 GPa, and the corresponding crystallization depth ranges from 7.64 to 13.4 km. The specific calculation results are listed in Table 2 and Online Materials[1] Table OM3.

The Ti-in-zircon thermometer has become an accurate and precise monitor of both igneous and metamorphic thermal history (Bloch et al. 2022; Fu et al. 2008; Schiller and Finger

Table 3. Crystallization conditions of amphibole and clinopyroxene from the Zhuyuan granodiorites

Mineral	Temperature (°C)	Pressure (GPa)	Depth (km)
Type-1 Cpx	1150–1191	0.48–0.75	18.1–28.4
Type-2 Cpx	1130–1192	0.40–0.84	15.3–31.7
Type-3 Cpx	1173–1211	0.38–0.61	14.2–23.0
Amphibole	744–814	0.20–0.35	7.64–13.4

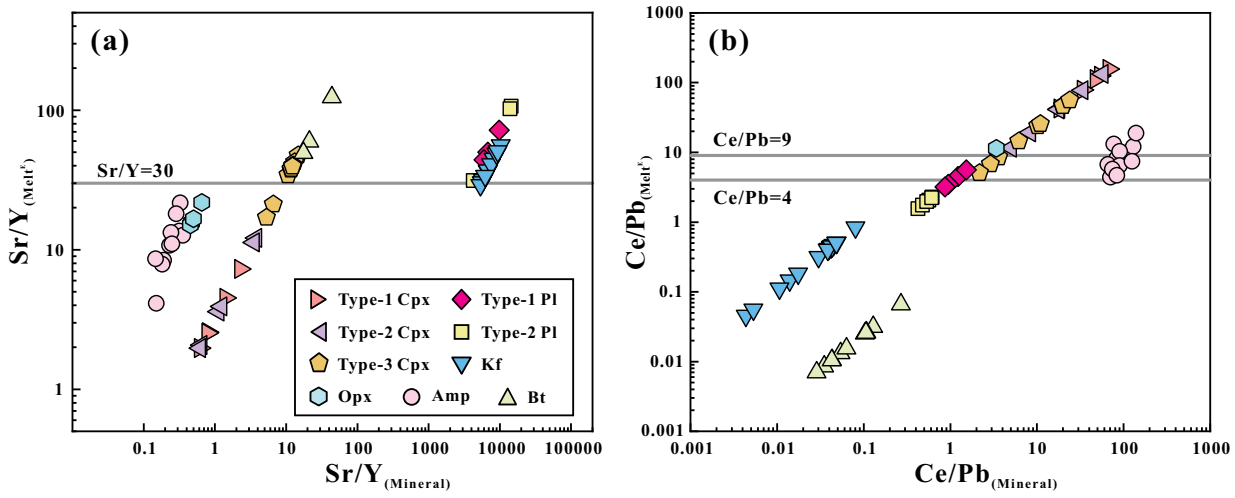

Figure 12. Sr/Y values of different minerals vs. those of the melts in equilibrium with them (**a**), and the melts with Sr/Y values higher than 30 are considered to have high-Sr/Y signature; Ce/Pb values of different minerals vs. those of the melts in equilibrium with them (**b**). The Ce/Pb value of mantle derived melt is generally >9, while that of shell derived melt is usually <4 (Hofmann et al. 1986; Sims and DePaolo 1997). (Color online.)

2019; Watson et al. 2006). Apparent temperatures for zircon crystallization for the Zhuyuan granodiorites were calculated using the Ti-in-zircon thermometer (Watson et al. 2006). We estimated the apparent peak temperature for the zircons from the Zhuyuan granodiorites (Xie et al. 2023), ranging from 721 to 787 °C (30 zircons; Online Materials[1] Table OM2). In addition, some of the higher apparent temperatures range from 893 to 989 °C (3 zircons).

The zircons from the Zhuyuan granodiorite show obvious negative Eu anomalies (0.01–0.64, Online Materials[1] Table OM2; Xie et al. 2023), indicating that they crystallized later than plagioclase or contemporaneously with plagioclase. Considering that Type-2 plagioclase belongs to the late-stage mineral assemblage, it is reasonable to assume that the crystallization temperatures of Type-2 plagioclase are close to, or overlap with, those of zircons. The water contents of the magma (Online Materials[1] Table OM3), from which the Type-2 plagioclase crystallized, are calculated using the plagioclase-liquid hygrometer of Waters and Lange (2015), for which the impact of the pressure is negligible, but the effect of the temperature is significant (Lange et al. 2009; Waters and Lange 2015). We have used the whole-rock compositions of our samples as proxies for the primitive melt compositions. However, the hygrometer we employed is insensitive to variations in liquid compositions and is thus well suited for our samples that have undergone an open-system crustal evolution. Assuming the maximum apparent temperatures for zircon crystallization, we calculate magmatic water contents ranging from 6.12–6.46 wt% based on rims of plagioclase with sieve texture and values ranging from 6.11–6.50 wt% for the Type-2 plagioclase. The use of the minimum zircon crystallization temperatures yielded values of 7.99–8.34 wt% for rims of plagioclase with sieve textures and 7.99–8.38 wt% for Type-2 plagioclase. Consequently, we conclude that the high-Sr/Y magma reservoir was hydrous (H_2O contents >4 wt%; Patiño Douce 1999; Collins et al. 2020) when late-stage plagioclase (Type-2 plagioclase) crystallized.

Crystal cargoes in the magmatic plumbing system

Based on the crystallization conditions of different minerals in the Zhuyan pluton and the compositions of equilibrium melts, we attempted to construct an open magmatic plumbing system model, which is illustrated in Figure 13. The melts in equilibrium with both Type-1 Cpx and Type-2 Cpx (Environments A and B) are likely indicative of extensive fractional crystallization resulting in a large range of Ni and Cr contents. In support of this interpretation, we note that amphiboles were formed at the expense of Cpx, likely in a peritectic reaction relationship (Figs. 3 and 5), and we speculate that both Type-1 Cpx and Type-2 Cpx are "antecrysts" that crystallized from separate mafic to intermediate magma batches. Our geobarometry data indicate that both Type-1 Cpx and Type-2 Cpx formed at depths of 15.3–31.7 km (Table 3; Online Materials[1] Table OM3), whereas crystal-melt equilibria (Environments C) indicate that the Type-3 Cpx cores are also likely antecrysts characterized by a more primitive rim overgrowth that was in disequilibrium with the host magmas. High-Cr and -Ni concentrations and X_{Mg} in the Type-3 Cpx rims indicate the overgrowth is the result of mafic magma replenishment (Figs. 5f and 7). The estimated depths where Type-3 Cpx crystallized vary from 14.2 to 23.0 km (Table 3). The relic Opx with a resorbed boundary is also defined by high-Ni and -Cr contents and is indicative of an antecryst origin (Environments D). The overgrowth of relic Opx by amphibole implies that Opx entered a hydrous magma reservoir.

The estimated depths at which amphiboles crystallized vary from 7.6 to 13.4 km (Table 3). There is no statistical overlap in terms of crystallization depths between amphiboles and pyroxenes, indicating that they may have crystallized at different magma reservoirs in the crust, and pyroxenes were overgrown by amphiboles in a magma reservoir at shallow crustal levels. The lobate boundary between amphibole and plagioclase (Fig. 3e), and the corroded grains of amphibole (Fig. 3g) indicate that there is a reactive relationship between amphibole and plagio-

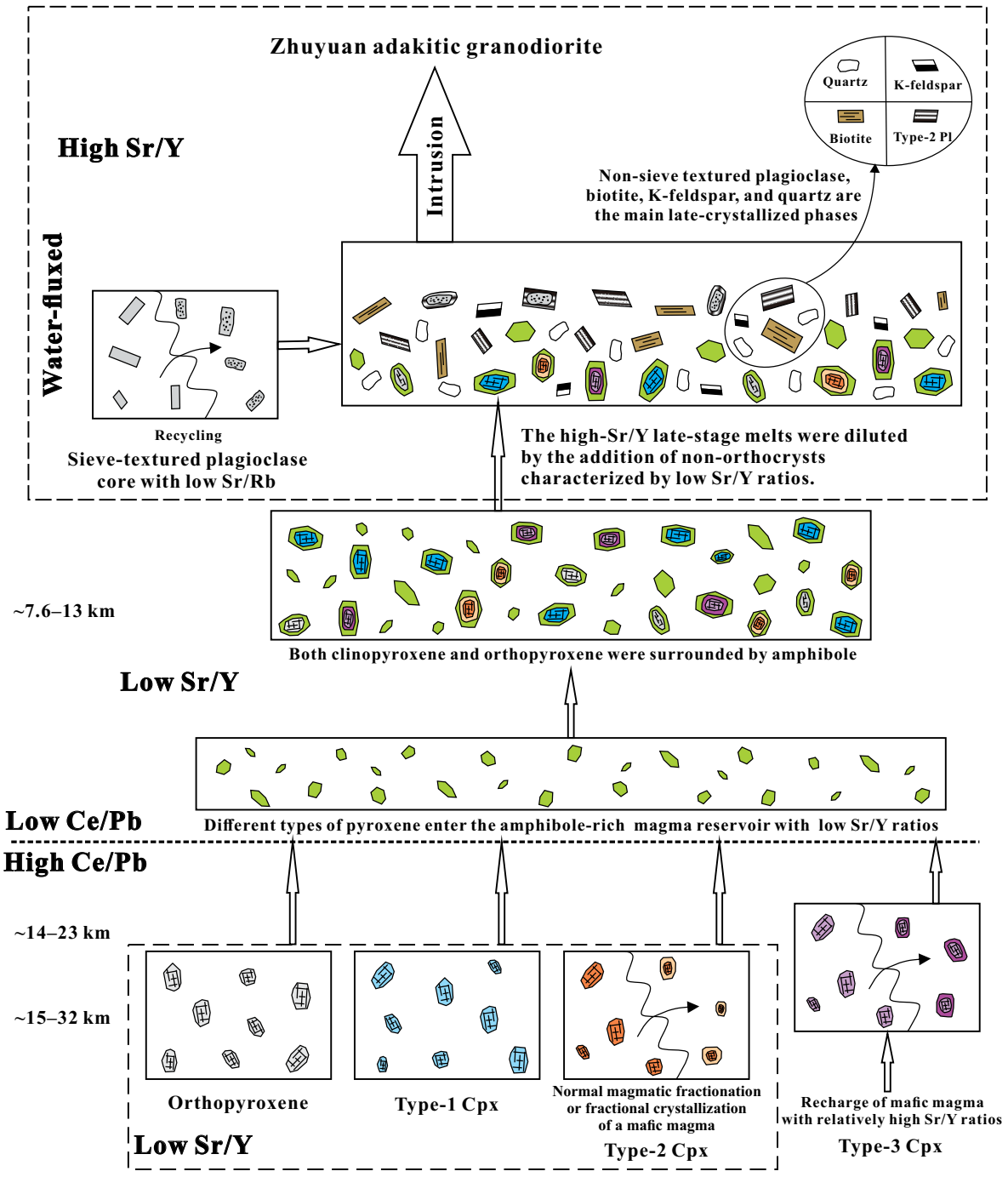

Figure 13. Schematic diagram showing the hypothetical magma conduit system used by magmas that formed the Zhuyuan adakitic granodiorites and the various possible mineral crystallization environments. (Color online.)

clase. In addition, some amphiboles display poikilitic textures with biotites (Fig. 3c), indicating that they crystallized from different melts. Considering the low Sr/Y values and relatively high-Ce/Pb values of the melts in equilibrium with both large and small amphiboles, it is likely that these amphiboles crystallized from other magma reservoirs that are compositionally different from the environments that crystallized the Type-2 plagioclase, Kfs, and biotite. Therefore, we tend to consider amphiboles as antecrysts.

The sieve-textured plagioclase core (Type-1 plagioclase) is likely an antecryst due to its resorbed and most calcic nature, and its equilibrium melt (Environments F) has lower Sr/Rb and Sr/Ba values and higher Ce/Pb values in comparison with melt in equilibrium with the Type-1 plagioclase rim.

We speculate that Environments G and H that crystallized Type-2 plagioclase, Bt, Kfs, and Qtz are similar due to similar Eu/Eu*, Sr/Y, and Ce/Pb values (Figs. 11–12; Tables 1–2). Furthermore, their petrography exhibits the characteristics of paragenetic mineral assemblages (Fig. 3). Thus, these four (Type-2 plagioclase, Bt, Kfs, and Qtz) can be reasonably interpreted as orthocrysts which crystallized during the late stage of magma evolution, which is also consistent with the petrographic observations (Fig. 3; Table 1).

Melts in equilibrium with pyroxenes collectively display low Sr/Y values, and it is unlikely that these melts developed adakitic signatures through crystal fractionation. Although hornblende fractionation may drive magmas toward high-Sr/Y values (Castillo et al. 1999), in this case, we would expect that the melts in equilibrium with the amphiboles would also gradually evolve toward higher Sr/Y values. Contrary to prediction, all melts in equilibrium with large (Type-1) and small (Type-2) amphiboles collectively have low Sr/Y values (4.13 to 21.6). From a whole-rock perspective, a negative correlation between $(Dy/Yb)_N$ and $(La/Yb)_N$ is expected for amphibole-dominant fractional crystallization (Davidson et al. 2007; He et al. 2011). However, the two ratios show a slight positive correlation for the Zhuyuan granodiorites (gray dashed line with an arrowhead in Online Materials[1] Fig. OM2a).

In summary, we identify several different magma batches (environments). Three types of Cpxs and Opx are antecrysts from mafic melts with low Sr/Y but high-Ce/Pb values. The different groups of amphibole testify to the presence of more than two different melts with low Sr/Y and medium Ce/Pb values. It is difficult to determine whether these amphiboles have genetic connections with the pyroxenes through fractional crystallization. Meanwhile, the antecrystic Type-1 plagioclase cores likely crystallized in the melt with a more calcic composition than Type-2 plagioclase. Finally, the late-stage orthocrysts, including the Type-2 plagioclase, Bt, Kfs, and Qtz were probably derived from an intermediate to felsic source with high-Sr/Y properties.

High-Sr/Y melts produced by anatexis of intermediate-felsic rocks under the water-fluxed condition

Experimental studies show that the fluid-absent breakdown of micas from the intermediate-felsic protoliths may produce melts with low Sr/Rb and Sr/Ba and notable negative Eu anomalies (Harris et al. 1993; Weinberg and Hasalová 2015; Zhou et al. 2020). This is consistent with the presence of K-feldspar as a coexisting peritectic phase in melts generated by muscovite and/or biotite dehydration melting (Harris et al. 1993). In comparison, water-fluxed melting of intermediate–felsic rocks (e.g., diorite, granodiorite, etc.) at mid-crustal levels (0.6–1.2 GPa) will generate felsic magmas with high Sr/Y (Reichardt and Weinberg 2012; Zhan et al. 2020). Water-fluxed melting (Amp + Pl + Qtz + vapor = melt), where preferential feldspar consumption over micas may leave an amphibole-rich residue in the source, leads to felsic melts expected to have positive Eu anomalies, low Rb contents, and high-Sr/Rb and -Sr/Ba values (Harris et al. 1993; Reichardt and Weinberg 2012). Simultaneously, these felsic melts may display high Al_2O_3 (>16 wt%), low $Fe_2O_3^T$ (<4.5 wt%), and elevated Sr concentrations while exhibiting HREE depletions (Beard and Lofgren 1991; Frost et al. 2016; Zhang et al. 2021).

We hypothesize that the resorbed, sieve-textured plagioclase (Type-1 plagioclase) core with a relatively high-Rb content (10.4–318 ppm) indicates an antecrystic origin (Table 1). By contrast, the high-Sr/Y melts in equilibrium with the Type-2 plagioclase display low Rb contents, high-Sr/Rb and -Sr/Ba values, and positive Eu anomalies, suggesting that the high-Sr/Y melts in equilibrium with them likely formed due to partial melting of intermediate to felsic rocks under water-fluxed conditions. This inference is consistent with the finding that Type-2 plagioclase crystallized under water-rich conditions (see section "Crystallization Conditions"). Therefore, the high-water contents of the melts in equilibrium with the Type-2 plagioclase most likely resulted from the anatexis of intermediate-felsic rocks under water-fluxed conditions.

Although the whole-rock composition is a mixture of multiple batches of magmas, the late-stage mineral assemblage still dominates the whole-rock compositions because the volume percentage of the rim of Type-1 plagioclase, Type-2 plagioclase + Bt + Kfs + Qtz is >75%. Therefore, the whole-rock compositions reflect the first-order characteristics of late-stage melting despite the presence of antecrysts, which function to dilute the high-Sr/Y bulk rock composition. In addition, whole-rock compositions display high Al_2O_3 (15.64–17.32 wt%) and low $Fe_2O_3^T$ (3.71–5.28 wt%) and show pronounced HREE depletions [$(La/Yb)_N$ = 15–21]. Meanwhile, we note that the addition of antecrystic mafic minerals resulted in higher concentrations of $Fe_2O_3^T$ and decreased Al_2O_3 in whole-rock compositions. Accordingly, the late-stage felsic melt typically has higher Al_2O_3, but lower $Fe_2O_3^T$ contents. However, melts produced by water-flux melting of intermediate to felsic rocks under 0.6–1.2 GPa are generally characterized by high Al_2O_3 (>16 wt%) and low $Fe_2O_3^T$ (<4.5 wt%) (Beard and Lofgren 1991; Frost et al. 2016), which coincide with late-stage melt compositions of the Zhuyuan granodiorites.

Moreover, the low Rb and high-Sr contents of the melts in equilibrium with the Type-2 plagioclase also argue against an extensive fractionation process, thus ruling out the possibility that the high-water content is caused by the high degrees of fractional crystallization (Wang et al. 2017). Accordingly, we conclude that the late-stage orthocryst assemblage represents the near-primary high-Sr/Y composition derived from the water-fluxed melting of intermediate to felsic source rocks. Meanwhile, the high-Sr/Y signal of felsic melts was diluted by magma recharge, leading to more mafic compositions in bulk.

Modeling for source rock compositions

To further elucidate the dilution of the high-Sr/Y properties of late-stage felsic melt by antecrysts with low-Sr/Y values and to identify the possible sources of these late-stage melts, we carried out simple quantitative simulations. We assume sample ZY17–8 (Opx free) to represent a melt composition that is least affected by the low-Sr/Y antecrysts, given that it is one of the samples with the highest SiO_2 contents (67.16 wt%) and relatively low Mg# value (50; Online Materials[1] Table OM2) (Xie et al. 2023). The proportion of various rock-forming minerals in the sample is estimated using mass balance calculations (Li et al. 2020b). The calculated results (Online Materials[1] Table OM7) are in good agreement with the petrographic observations. We

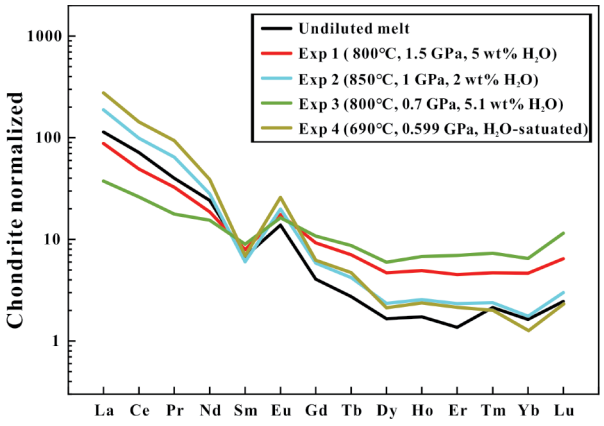

Figure 14. Chondrite normalized REE patterns of calculated intermediate felsic sources (color lines) of the high-Sr/Y undiluted melt of the Zhuyuan granodiorites under different conditions. The color lines correspond to different experiments listed in Online Materials[1] Table OM7. The source rocks corresponding to Exp 1 to 4 are garnet-bearing semi-pelitic metasedimentary gneiss, orthogneiss, garnet-bearing metasedimentary gneiss, and biotite tonalite. (Color online.)

estimate the interstitial magma compositions (i.e., the "undiluted melt") by removing the mass of antecrysts. After deducting the intermediate-mafic antecrysts, the remaining bulk composition shows high-SiO_2 content (70.33 wt%), low Mg# value (31.4), and significantly increased Sr content (555 ppm) and Sr/Y value (132). By comparing the whole-rock Sr/Y value (36.3) of sample ZY17–8, we confirm that the adakitic signals of the high-Sr/Y melts are significantly weakened by the incorporation of intermediate-mafic antecrysts. Thus, antecryst entrainment is crucial for understanding the geochemical diversity of granitic magmas with an adakitic signature, and whole-rock compositions of granitoids probably deviate remarkably from the original melt compositions (Werts et al. 2020).

To quantitatively simulate the nature of the source rock, we assumed that the high-Sr/Y "undiluted melt" calculated based on sample ZY17–8 with the highest Zr/Hf value is the near-primary melt derived from partial melting of intermediate-felsic source rock. When the residual solid phase and melt fraction (i.e., the degree of partial melting) can be reasonably constrained, the trace element compositions of the source rock can be calculated from known melt compositions using the batch melting model of Shaw (1970):

$$C_0^i = C_L^i * [D_{Bulk}^i + F * (1 - D_{Bulk}^i)]$$

where C_0^i and C_L^i represent the concentration of element i in the source rock and melt, respectively; F is the melt fraction of source rock; and D_{Bulk}^i is the bulk partition coefficient of element i, which is the sum of the partition coefficient (D) for each mineral multiplied by the weight percentage of corresponding mineral in the residual solid phase ($D_{Bulk}^i = D_S^i * W_S$).

We compared the major elements of the undiluted melt with that of experimental melts derived from the partial melting of a range of crustal protoliths compiled by Gao et al. (2016), Weinberg and Hasalová (2015), and Zhan et al. (2020). To find the best matching experimental melt compositions, the sum of the square of the deviations of each major element oxides between experimental melts and undiluted melt was calculated. Based on the earlier discussion on water-fluxed melting, only the melting experiments of intermediate-felsic source rocks under water-presence conditions are considered here. We report the four best matching experimental melts (the sum of squared deviations is <10) and the corresponding partial melting pressures, melt fractions, and proportion of residual solid phases (Experiments 1–4 in Online Materials[1] Table OM7).

We also explore the trace element composition of the source rocks (e.g., REE, Sr, and Y) of undiluted melt (inferred from sample ZY17–8) using compositionally appropriate mineral partition coefficients (Online Materials[1] Table OM7) and the batch melting equation. The calculated trace element compositions under different melting conditions corresponding to the four experiments are listed in Online Materials[1] Table OM7 and are plotted in Figure 14. The modeling results show that different source rocks may have different implications for constraining the derivation of high-Sr/Y granites.

We find that the calculated trace elements of intermediate-felsic sources corresponding to different melting conditions are characterized by significant positive Eu anomalies (1.66–3.96), indicating that the plagioclase accumulation in the source rocks is particularly important for melting to produce high-Sr/Y melt. This is consistent with the interpretations proposed by Shi et al. (2022) and Wang et al. (2022). In addition, we have obtained the following results.

(1) In the experimental runs under high-pressure conditions (Exp 1, 800 °C, 1.5 GPa, 5 wt% H_2O; Koester et al. 2002), the partial melting degree of source rocks is relatively low (21%). The calculated source rock shows a low Sr/Y value (21.9), which is mainly due to the fact that the source rock contains a considerable proportion of garnet (Grt) and amphibole. Therefore, for Exp 1 to produce the high-Sr/Y melt, it is necessary to have a significant amount of residual Y-rich minerals dominated by Grt in the source.

(2) In the experimental runs under moderate pressure conditions (Exp 2, 850 °C, 1 GPa, 2 wt% H_2O; García-Arias et al. 2012), the partial melting degree of source rocks is relatively high (61%), with minor Grt in the residues (<1 wt%). Our modeling result for source rock exhibits a relatively high-Sr/Y value (98.9), which is most likely due to the high abundance of feldspar but the low abundance of Grt in the source. Moreover, the high-Sr/Y signal of the partial melt is mainly attributed to significant melting of feldspar in the source rocks, releasing large amounts of Sr into the melt.

(3) In the moderate-low pressure melting experiment of Grt-bearing metasedimentary gneiss (Exp 3, 800 °C, 0.7 GPa, 5.1 wt% H_2O; Ward et al. 2008), the degree of partial melting in the source rocks is relatively high (67%). Feldspar is absent in the residues, but some Y-rich minerals (Grt + Amp) are retained. In addition, the calculated source rock shows the least obvious positive Eu anomaly (Eu/Eu* = 1.66) and has a much lower Sr content (183 ppm) and Sr/Y value (12.6). These results indicate that the high-Sr/Y signal of the partial melt requires concurrent feldspar melting and retention of an Y-rich mineral in the residue.

(4) In the low-pressure melting experiment of biotite tonalite

(Exp 4, 690 °C, 0.599 GPa, H_2O-saturated; Watkins et al. 2007), the moderate degree of partial melting (32%) produces a melt with major elements comparable to undiluted melt of sample ZY17–8. The calculated trace elements of this biotite tonalite (source rock) are characterized by strongly fractionated REE patterns (Fig. 14), strong positive Eu anomalies, and high $(La/Yb)_N$ (265) and Sr/Y (191) values. Furthermore, Y-rich minerals are absent in the residues of Exp 4, and some feldspar is present. Therefore, the high-Sr/Y signal of the partial melt corresponding to Exp 4 is completely inherited from the source rock, mainly through the melting of large amounts of feldspar under water-saturated conditions.

In summary, for intermediate-felsic sources, water-present to water-saturated partial melting at high to low pressures (corresponding to 0.599 to 1.5 GPa) may produce the high-Sr/Y and $-(La/Yb)_N$ signatures of the Zhuyuan granodiorites. We also note that high-Sr/Y and $-(La/Yb)_N$ values are produced even when the source rock contains no or very little Y-rich minerals (Grt + Amp). However, when Y-rich minerals are enriched in source rocks, high-Sr/Y melts may also be produced by melting a large amount of feldspar while retaining considerable amounts of Y-rich minerals in the sources. Thus, we suggest that the Zhuyuan high-Sr/Y melts were produced under various pressure conditions, and not limited to high pressures (>1.5 GPa). Previous studies have also confirmed that felsic melt with adakitic signatures can be generated at much lower pressures (0.6–1.2 GPa, e.g., Zhan et al. 2020). Accordingly, high-Sr/Y adakitic granites cannot be directly used to infer the thickness of the continental crust when the source is a felsic to intermediate protolith melted under water-fluxed conditions.

Implications

Our study highlights that the adakitic signatures in plutonic rocks are not only significantly influenced by the stability (e.g., under high-pressure conditions) and modal abundance of source residual minerals (Moyen 2009), but also by the variations in source lithology and water content (Johnson et al. 2017; Ma et al. 2015; Pourteau et al. 2020). For example, magmas with adakitic affinity can be generated by water-fluxed melting of intermediate to felsic rocks under various pressures (Moyen 2009). In addition, antecryst recycling processes in granitic magma systems are common (Barnes et al. 2019; Oppenheim et al. 2021). Injection by diverse magma batches with various types of non-orthocrysts could significantly obscure the evolutionary path of the primary magmas. Our study clearly reveals that the high-Sr/Y signal of primary adakitic melts can be diluted by the addition of non-orthocrysts or other batches of melts with low Sr/Y values. From this perspective, estimates of paleo-crustal thickness based on whole-rock granitic compositions (Profeta et al. 2015; Hu et al. 2017) should be considered with caution due to the possibility of open-system behavior that may have affected original melt compositions.

Acknowledgments

We express our sincere gratitude to Hongwu Xu and Associate Editor Callum Hetherington for their efficient handling of our manuscript and valuable insights. We also thank Reviewers Kenneth Johnson and John Adam for their constructive comments, which have greatly contributed to the improvement of our paper. Additionally, we thank Zhao-Hua Luo, Yuan-Yuan Xiao and Qiong-Yao Zhan for assistance with many helpful discussions.

Funding

This work was jointly funded by the State Key Program of National Natural Science of China (Grant 41730426), the National Natural Science Foundation of China (Grants 41872066, 41872082, and 41702069), the Fundamental Research Funds for the Central Universities of China (2652018121), and the Open Research Funds for GPMR (Grant GPMR201509).

References cited

Bach, P., Smith, I.E.M., and Malpas, J.G. (2012) The origin of garnets in andesitic rocks from the Northland Arc, New Zealand, and their implication for sub-arc processes. Journal of Petrology, 53, 1169–1195, https://doi.org/10.1093/petrology/egs012.

Barnes, C.G., Werts, K., Memeti, V., and Ardill, K. (2019) Most granitoid rocks are cumulates: Deductions from hornblende compositions and zircon saturation. Journal of Petrology, 60, 2227–2240, https://doi.org/10.1093/petrology/egaa008.

Beard, J.S. and Lofgren, G.E. (1991) Dehydration melting and water-saturated melting of basaltic and andesitic greenstones and amphibolites at 1, 3, and 6. 9 kb. Journal of Petrology, 32, 365–401, https://doi.org/10.1093/petrology/32.2.365.

Bédard, J.H. (2001) Parental magmas of the Nain Plutonic Suite anorthosites and mafic cumulates: A trace element modelling approach. Contributions to Mineralogy and Petrology, 141, 747–771, https://doi.org/10.1007/s004100100268.

Bindeman, I.N., Davis, A.M., and Drake, M.J. (1998) Ion microprobe study of plagioclase-basalt partition experiments at natural concentration levels of trace elements. Geochimica et Cosmochimica Acta, 62, 1175–1193, https://doi.org/10.1016/S0016-7037(98)00047-7.

Bloch, E.M., Jollands, M.C., Tollan, P., Plane, F., Bouvier, A.S., Hervig, R., Berry, A.J., Zaubitzer, C., Escrig, S., Müntener, O., and others. (2022) Diffusion anisotropy of Ti in zircon and implications for Ti-in-zircon thermometry. Earth and Planetary Science Letters, 578, 117317, https://doi.org/10.1016/j.epsl.2021.117317.

Blundy, J. and Cashman, K. (2008) Petrologic reconstruction of magmatic system variables and processes. Reviews in Mineralogy and Geochemistry, 69, 179–239, https://doi.org/10.2138/rmg.2008.69.6.

Brackman, A.J. and Schwartz, J.J. (2022) The formation of high-Sr/Y plutons in cordilleran-arc crust by crystal accumulation and melt loss. Geosphere, 18, 370–393, https://doi.org/10.1130/GES02400.1.

Burney, D., Peate, D.W., Riishuus, M.S., and Ukstins, I.A. (2020) Reconstructing the plumbing system of an off-rift primitive alkaline tuya (Vatnafell, Iceland) using geothermobarometry and CSDs. Journal of Volcanology and Geothermal Research, 399, 106914, https://doi.org/10.1016/j.jvolgeores.2020.106914.

Calmus, T., Aguillon-Robles, A., Maury, R.C., Bellon, H., Benoit, M., Cotten, J., Bourgois, J., and Michaud, F. (2003) Spatial and temporal evolution of basalts and magnesian andesites (bajaites) from Baja California, Mexico: The role of slab melts. Lithos, 66, 77–105, https://doi.org/10.1016/S0024-4937(02)00214-1.

Cashman, K.V., Sparks, R.S., and Blundy, J.D. (2017) Vertically extensive and unstable magmatic systems: A unified view of igneous processes. Science, 355, eaag3055, https://doi.org/10.1126/science.aag3055.

Castillo, P.R. (2012) Adakite petrogenesis. Lithos, 134-135, 304–316, https://doi.org/10.1016/j.lithos.2011.09.013.

Castillo, P.R., Janney, P.E., and Solidum, R.U. (1999) Petrology and geochemistry of Camiguin Island, southern Philippines: Insights to the source of adakites and other lavas in a complex arc setting. Contributions to Mineralogy and Petrology, 134, 33–51, https://doi.org/10.1007/s004100050467.

Chen, S., Niu, Y., Li, J., Sun, W., Zhang, Y., Hu, Y., and Shao, F. (2016) Syn-collisional adakitic granodiorites formed by fractional crystallization: Insights from their enclosed mafic magmatic enclaves (MMEs) in the Qumushan pluton, North Qilian Orogen at the northern margin of the Tibetan Plateau. Lithos, 248-251, 455–468, https://doi.org/10.1016/j.lithos.2016.01.033.

Clemens, J.D. and Stevens, G. (2012) What controls chemical variation in granitic magmas? Lithos, 134-135, 317–329, https://doi.org/10.1016/j.lithos.2012.01.001.

Collins, W.J., Murphy, J.B., Johnson, T.E., and Huang, H. (2020) Critical role of water in the formation of continental crust. Nature Geoscience, 13, 331–338, https://doi.org/10.1038/s41561-020-0573-6.

Davidson, J., Turner, S., Handley, H., Macpherson, C., and Dosseto, A. (2007) Amphibole "sponge" in arc crust? Geology, 35, 787–790, https://doi.org/10.1130/G23637A.1.

Defant, M.J. and Drummond, M.S. (1990) Derivation of some modern arc magmas by melting of young subducted lithosphere. Nature, 347, 662–665, https://doi.org/10.1038/347662a0.

Elkins, L.J., Gaetani, G.A., and Sims, K.W.W. (2008) Partitioning of U and Th during garnet pyroxenite partial melting: Constraints on the source of alkaline ocean island basalts. Earth and Planetary Science Letters, 265, 270–286, https://doi.org/10.1016/j.epsl.2007.10.034.

Ewart, A. and Griffin, W.L. (1994) Application of proton-microprobe data to trace-element partitioning in volcanic-rocks. Chemical Geology, 117, 251–284, https://doi.org/10.1016/0009-2541(94)90131-7.

Foster, M.D. (1960) Interpretation of the composition of trioctahedral micas. U.S. Geological Survey Professional Paper, 354, 1–49, https://doi.org/10.3133/pp354B.

Frost, C.D., Swapp, S.M., Frost, B.R., Finley-Blasi, L., and Fitz-Gerald, D.B. (2016) Leucogranites of the Teton Range, Wyoming: A record of Archean collisional orogeny. Geochimica et Cosmochimica Acta, 185, 528–549, https://doi.org/10.1016/j.

gca.2015.12.015.
Fu, B., Page, F.Z., Cavosie, A.J., Fournelle, J., Kita, N.T., Lackey, J.S., Wilde, S.A., and Valley, J.W. (2008) Ti-in-zircon thermometry: Applications and limitations. Contributions to Mineralogy and Petrology, 156, 197–215, https://doi.org/10.1007/s00410-008-0281-5.
Gao, P., Zheng, Y.F., and Zhao, Z.F. (2016) Experimental melts from crustal rocks: A lithochemical constraint on granite petrogenesis. Lithos, 266–267, 133–157, https://doi.org/10.1016/j.lithos.2016.10.005.
García-Arias, M., Corretgé, L.G., and Castro, A. (2012) Trace element behavior during partial melting of Iberian orthogneisses: An experimental study. Chemical Geology, 292-293, 1–17, https://doi.org/10.1016/j.chemgeo.2011.10.024.
Graham, B., Dunning, G., and Leitch, A. (2020) Magma mushes of the Fogo Island Batholith: A study of magmatic processes at multiple scales. Journal of Petrology, 61, egaa097, https://doi.org/10.1093/petrology/egaa097.
Guo, F., Nakamuru, E., Fan, W., Kobayoshi, K., and Li, C. (2007) Generation of Palaeocene adakitic andesites by magma mixing: Yanji Area, NE China. Journal of Petrology, 48, 661–692, https://doi.org/10.1093/petrology/egl077.
Harris, N., Massey, J., and Inger, S. (1993) The role of fluids in the formation of High Himalayan leucogranites. Special Publication—Geological Society of London, 74, 391–400, https://doi.org/10.1144/GSL.SP.1993.074.01.26.
He, Y., Li, S., Hoefs, J., Huang, F., Liu, S.-A., and Hou, Z. (2011) Post-collisional granitoids from the Dabie orogen: New evidence for partial melting of a thickened continental crust. Geochimica et Cosmochimica Acta, 75, 3815–3838, https://doi.org/10.1016/j.gca.2011.04.011.
Higgins, M.D. (1996) Crystal size distributions and other quantitative textural measurements in lavas and tuff from Egmont volcano (Mt. Taranaki), New Zealand. Bulletin of Volcanology, 58, 194–204, https://doi.org/10.1007/s004450050135.
Higgins, O., Sheldrake, T., and Caricchi, L. (2022) Machine learning thermobarometry and chemometry using amphibole and clinopyroxene: A window into the roots of an arc volcano (Mount Liamuiga, Saint Kitts). Contributions to Mineralogy and Petrology, 177, 1–22.
Hofmann, A.W., Jochum, K.P., Seufert, M., and White, W.M. (1986) Nb and Pb in oceanic basalts: New constraints on mantle evolution. Earth and Planetary Science Letters, 79, 33–45, https://doi.org/10.1016/0012-821X(86)90038-5.
Holland, T. and Blundy, J. (1994) Non-ideal interactions in calcic amphiboles and their bearing on amphibole–plagioclase thermometry. Contributions to Mineralogy and Petrology, 116, 433–447, https://doi.org/10.1007/BF00310910.
Hollings, P., Sievwright, R.H., Buret, Y., Wilkinson, J.J., Loader, M.A., and Nathwani, C.L. (2020) Multi-stage arc magma evolution recorded by apatite in volcanic rocks. Geology, 48, 323–327.
Hu, F., Ducea, M.N., Liu, S., and Chapman, J.B. (2017) Quantifying crustal thickness in continental collisional belts: Global perspective and a geologic application. Scientific Reports, 7, 7058, https://doi.org/10.1038/s41598-017-07849-7.
Hu, J., Li, X., Xu, J., Mo, X., Wang, F., Yu, H., Shan, W., Xing, H., Huang, X., and Dong, G. (2019) Generation of coeval metaluminous and muscovite-bearing peraluminous granitoids in the same composite pluton in West Qinling, NE Tibetan Plateau. Lithos, 344-345, 374–392, https://doi.org/10.1016/j.lithos.2019.06.034.
Humphreys, M.C.S., Cooper, G.F., Zhang, J., Loewen, M., Kent, A.J.R., Macpherson, C.G., and Davidson, J.P. (2019) Unravelling the complexity of magma plumbing at Mount St. Helens: A new trace element partitioning scheme for amphibole. Contributions to Mineralogy and Petrology, 174, 9, https://doi.org/10.1007/s00410-018-1543-5.
Jerram, D.A. and Martin, V.M. (2008) Understanding crystal populations and their significance through the magma plumbing system. Special Publication—Geological Society of London, 304, 133–148, https://doi.org/10.1144/SP304.7.
Jerram, D.A., Dobson, K.J., Morgan, D.J., and Pankhurst, M.J. (2018) The petrogenesis of magmatic systems: Using igneous textures to understand magmatic processes, volcanic and igneous plumbing systems. Elsevier, 191–229.
Ji, Z., Ge, W., Yang, H., Tian, D., Chen, H., and Zhang, Y. (2018) Late Carboniferous–Early Permian high- and low-Sr/Y granitoids of the Xing'an Block, northeastern China: Implications for the late Paleozoic tectonic evolution of the eastern Central Asian Orogenic Belt. Lithos, 322, 179–196, https://doi.org/10.1016/j.lithos.2018.10.014.
Johnson, T.E., Brown, M., Gardiner, N.J., Kirkland, C.L., and Smithies, R.H. (2017) Earth's first stable continents did not form by subduction. Nature, 543, 239–242, https://doi.org/10.1038/nature21383.
Kay, R.W. (1978) Aleutian magnesian andesites: Melts from subducted Pacific ocean crust. Journal of Volcanology and Geothermal Research, 4, 117–132, https://doi.org/10.1016/0377-0273(78)90032-X.
Koester, E., Pawley, A.R., Fernandes, L.A.D., Porcher, C.C., and Soliani, J.R.E. (2002) Experimental melting of cordierite gneiss and the petrogenesis of syntranscurrent peralumnious granites in southern Brazil. Journal of Petrology, 43, 1595–1616, https://doi.org/10.1093/petrology/43.8.1595.
Lange, R.A., Frey, H.M., and Hector, J. (2009) A thermodynamic model for the plagioclase-liquid hygreometer/thermometer. American Mineralogist, 94, 494–506, https://doi.org/10.2138/am.2009.3011.
Leake, B.E., Woolley, A.R., Arps, C.E.S., Birch, W.D., Gilbert, M.C., Grice, J.D., Hawthorne , J.D., Kato, A., Kisch, H.J., Krivovichev, V.G., and others. (1997) Nomenclature of amphiboles: Report of the Subcommittee on Amphiboles of the International Mineralogical Association Commission on New Minerals and Mineral Names. Mineralogical Magazine, 61, 295–310, https://doi.org/10.1180/minmag.1997.061.405.13.
Li, X., Mo, X., Huang, X., Dong, G., Yu, X., Luo, M., and Liu, Y. (2015) U-Pb zircon geochronology, geochemical and Sr-Nd-Hf isotopic compositions of the Early Indosinian Tongren Pluton in West Qinling: Petrogenesis and geodynamic implications. Journal of Asian Earth Sciences, 97, 38–50, https://doi.org/10.1016/j.jseaes.2014.10.017.
Li, X., Zhang, C., Almeev, R.R., and Holtz, F. (2020a) GeoBalance: An Excel VBA program for mass balance calculation in geosciences. Chemie der Erde, 80, 125629, https://doi.org/10.1016/j.chemer.2020.125629.
Li, X., Zhang, C., Behrens, H., and Holtz, F. (2020b) Calculating amphibole formula from electron microprobe analysis data using a machine learning method based on principal components regression. Lithos, 362-363, 105469, https://doi.org/10.1016/j.lithos.2020.105469.
Lu, Y. (2005) GeoKit-A geochemical toolkit for Microsoft Excel. Geochimica, 35, 459–464 (in Chinese with English abstract).
Luo, B., Zhang, H., and Lü, X. (2012) U–Pb zircon dating, geochemical and Sr-Nd-Hf isotopic compositions of Early Indosinian intrusive rocks in West Qinling, central China: Petrogenesis and tectonic implications. Contributions to Mineralogy and Petrology, 164, 551–569, https://doi.org/10.1007/s00410-012-0748-2.
Ma, Q., Zheng, J.P., Xu, Y.G., Griffin, W.L., and Zhang, R.S. (2015) Are continental "adakites" derived from thickened or foundered lower crust? Earth and Planetary Science Letters, 419, 125–133, https://doi.org/10.1016/j.epsl.2015.02.036.
Macpherson, C.G., Dreher, S.T., and Thirlwall, M.F. (2006) Adakites without slab melting: High pressure differentiation of island arc magma, Mindanao, the Philippines. Earth and Planetary Science Letters, 243, 581–593, https://doi.org/10.1016/j.epsl.2005.12.034.
Marsh, B.D. (1988) Crystal size distribution (CSD) in rocks and the kinetics and dynamics of crystallization. Contributions to Mineralogy and Petrology, 99, 277–291, https://doi.org/10.1007/BF00375362.
Martin, H., Smithies, R.H., Rapp, R., Moyen, J.F., and Champion, D. (2005) An overview of adakite, tonalite-trondhjemite-granodiorite (TTG), and sanukitoid: Relationships and some implications for crustal evolution. Lithos, 79, 1–24, https://doi.org/10.1016/j.lithos.2004.04.048.
Miller, J.S., Matzel, J.E.P., Miller, C.F., Burgess, S.D., and Miller, R.B. (2007) Zircon growth and recycling during the assembly of large, composite arc plutons. Journal of Volcanology and Geothermal Research, 167, 282–299, https://doi.org/10.1016/j.jvolgeores.2007.04.019.
Morgan, D.J., Jerram, D.A., Chertkoff, D.G., Davidson, J.P., Pearson, D.G., Kronz, A., and Nowell, G.M. (2007) Combining CSD and isotopic microanalysis: Magma supply and mixing processes at Stromboli Volcano, Aeolian Islands, Italy. Earth and Planetary Science Letters, 260, 419–431, https://doi.org/10.1016/j.epsl.2007.05.037.
Morimoto, N., Fabries, J., Ferguson, A.K., Ginzburg, I.V., Ross, M., Seifert, F.A., Zussman, J., Aoki, K., and Gottardi, G. (1988) Nomenclature of pyroxenes. Mineralogical Magazine, 52, 535–550, https://doi.org/10.1180/minmag.1988.052.367.15.
Moyen, J.-F. (2009) High Sr/Y and La/Yb ratios: The meaning of the "adakitic signature". Lithos, 112, 556–574, https://doi.org/10.1016/j.lithos.2009.04.001.
Nachit, H., Ibhi, A., Abia, E.H., and Ben Ohoud, M. (2005) Discrimination between primary magmatic biotites, reequilibrated biotites and neoformed biotites. Comptes Rendus Geoscience, 337, 1415–1420, https://doi.org/10.1016/j.crte.2005.09.002.
Namur, O., Montalbano, S., Bolle, O., and Vander Auwera, J. (2020) Petrology of the April 2015 eruption of Calbuco Volcano, Southern Chile. Journal of Petrology, 61, egaa084, https://doi.org/10.1093/petrology/egaa084.
Nandedkar, R.H., Hürlimann, N., Ulmer, P., and Müntener, O. (2016) Amphibole-melt trace element partitioning of fractionating calc-alkaline magmas in the lower crust: An experimental study. Contributions to Mineralogy and Petrology, 171, 71, https://doi.org/10.1007/s00410-016-1278-0.
Nash, P.W. and Crecraft, H.R. (1985) Partition coefficients for trace elements in silicic magmas. Geochimica et Cosmochimica Acta, 49, 2309–2322, https://doi.org/10.1016/0016-7037(85)90231-5.
Neave, D.A. and Putirka, K.D. (2017) A new clinopyroxene-liquid barometer, and implications for magma storage pressures under Icelandic rift zones. American Mineralogist, 102, 777–794, https://doi.org/10.2138/am-2017-5968.
Neave, D.A., Bali, E., Guðfinnsson, G.H., Halldórsson, S.A., Kahl, M., Schmidt, A.-S., and Holtz, F. (2019) Clinopyroxene-liquid equilibria and geothermobarometry in natural and experimental tholeiites: The 2014–2015 Holuhraun eruption, Iceland. Journal of Petrology, 60, 1653–1680, https://doi.org/10.1093/petrology/egz042.
Oppenheim, L.F., Memeti, V., Barnes, C.G., Chambers, M., Krause, J., and Esposito, R. (2021) Feldspar recycling across magma mush bodies during the voluminous Half Dome and Cathedral Peak stages of the Tuolumne intrusive complex, Yosemite National Park, California, U.S.A. Geosphere, 17, 322–351, https://doi.org/10.1130/GES02286.1.
Ou, Q., Wang, Q., Wyman, D.A., Zhang, H., Yang, J., Zeng, J., Hao, L., Chen, Y., Liang, H., and Qi, Y. (2017) Eocene adakitic porphyries in the central-northern Qiangtang Block, central Tibet: Partial melting of thickened lower crust and implications for initial surface uplifting of the plateau. Journal of Geophysical Research. Solid Earth, 122, 1025–1053, https://doi.org/10.1002/2016JB013259.
Paterson, S., Memeti, V., Mundil, R., and Žák, J. (2016) Repeated, multiscale, magmatic erosion and recycling in an upper-crustal pluton: Implications for magma chamber dynamics and magma volume estimates. American Mineralogist, 101, 2176–2198, https://doi.org/10.2138/am-2016-5576.

Patiño Douce, A.E. (1999) What do experiments tell us about the relative contributions of crust and mantle to the origin of granitic magmas? Special Publication—Geological Society of London, 168, 55–75, https://doi.org/10.1144/GSL.SP.1999.168.01.05.
Pichavant, M. and Macdonald, R. (2007) Crystallization of primitive basaltic magmas at crustal pressures and genesis of the calc-alkaline igneous suite: Experimental evidence from St. Vincent, Lesser Antilles arc. Contributions to Mineralogy and Petrology, 154, 535–558, https://doi.org/10.1007/s00410-007-0208-6.
Pourteau, A., Doucet, L.S., Blereau, E.R., Volante, S., Johnson, T.E., Collins, W.J., Li, Z.-X., and Champion, D.C. (2020) TTG generation by fluid-fluxed crustal melting: Direct evidence from the Proterozoic Georgetown Inlier, NE Australia. Earth and Planetary Science Letters, 550, 116548, https://doi.org/10.1016/j.epsl.2020.116548.
Price, R.C., Gamble, J.A., Smith, I.E.M., Maas, R., Waight, T., Stewart, R.B., and Woodhead, J. (2012) The anatomy of an Andesite Volcano: A time-stratigraphic study of andesite petrogenesis and crustal evolution at Ruapehu Volcano, New Zealand. Journal of Petrology, 53, 2139–2189, https://doi.org/10.1093/petrology/egs050.
Profeta, L., Ducea, M.N., Chapman, J.B., Paterson, S.R., Gonzales, S.M., Kirsch, M., Petrescu, L., and DeCelles, P.G. (2015) Quantifying crustal thickness over time in magmatic arcs. Scientific Reports, 5, 17786, https://doi.org/10.1038/srep17786.
Putirka, K.D. (2008) Thermometers and barometers for volcanic systems. Reviews in Mineralogy and Geochemistry, 69, 61–120, https://doi.org/10.2138/rmg.2008.69.3.
Putirka, K. (2016) Amphibole thermometers and barometers for igneous systems and some implications for eruption mechanisms of felsic magmas at arc volcanoes. American Mineralogist, 101, 841–858, https://doi.org/10.2138/am-2016-5506.
Reichardt, H. and Weinberg, R.F. (2012) Hornblende Chemistry in meta- and diatexites and its retention in the source of leucogranites: An example from the Karakoram Shear Zone, NW India. Journal of Petrology, 53, 1287–1318, https://doi.org/10.1093/petrology/egs017.
Schiller, D. and Finger, F. (2019) Application of Ti-in-zircon thermometry to granite studies: Problems and possible solutions. Contributions to Mineralogy and Petrology, 174, 51, https://doi.org/10.1007/s00410-019-1585-3.
Schnetzler, C.C. and Philpotts, J.A. (1970) Partition coefficients of rare-earth elements between igneous matrix material and rock-forming mineral phenocrysts–II. Geochimica et Cosmochimica Acta, 34, 331–340, https://doi.org/10.1016/0016-7037(70)90110-9.
Shaw, D.M. (1970) Trace element fractionation during anatexis. Geochimica et Cosmochimica Acta, 34, 237–243, https://doi.org/10.1016/0016-7037(70)90009-8.
Shen, Y., Zheng, Y.-C., Hou, Z.-Q., Zhang, A.-P., Huizenga, J.M., Wang, Z.-X., and Wang, L. (2021) Petrology of the Machangqing Complex in Southeastern Tibet: Implications for the genesis of potassium-rich adakite-like intrusions in collisional zones. Journal of Petrology, 62, egab066, https://doi.org/10.1093/petrology/egab066.
Shi, H., Xia, Y., Xu, X., Zhu, J., and He, J. (2022) Crystal-melt separation of the Cretaceous volcanic-plutonic complex in SE China: High Sr/Y rocks generated by plagioclase accumulation. Lithos, 430-431, 106848, https://doi.org/10.1016/j.lithos.2022.106848.
Shimizu, K., Liang, Y., Sun, C., Jackson, C.R.M., and Saal, A.E. (2017) Parameterized lattice strain models for REE partitioning between amphibole and silicate melt. American Mineralogist, 102, 2254–2267, https://doi.org/10.2138/am-2017-6110.
Sims, K.W.W. and DePaolo, D.J. (1997) Inferences about mantle magma sources from incompatible element concentration ratios in oceanic basalts. Geochimica et Cosmochimica Acta, 61, 765–784, https://doi.org/10.1016/S0016-7037(96)00372-9.
Sisson, T.W. and Grove, T.L. (1993) Experimental investigations of the role of H_2O in calc-alkaline differentiation and subduction zone magmatism. Contributions to Mineralogy and Petrology, 113, 143–166, https://doi.org/10.1007/BF00283225.
Smith, J.V. (1974) Crystal structure and physical properties. Feldspar Minerals, 1, 625. Springer.
Stern, C.R. and Kilian, R. (1996) Role of the subducted slab, mantle wedge and continental crust in the generation of adakites from the Andean Austral Volcanic Zone. Contributions to Mineralogy and Petrology, 123, 263–281, https://doi.org/10.1007/s004100050155.
Streckeisen, A.L. (1976) Classification of the common igneous rocks by means of their chemical composition: A provisional attempt. Neues Jahrbuch für Mineralogie Monatshefte, 1, 1–15.
Sun, S.S. and McDonough, W.F. (1989) Chemical and isotopic systematics of oceanic basalts: Implications for mantle composition and processes. Special Publication—Geological Society of London, 42, 313–345, https://doi.org/10.1144/GSL.SP.1989.042.01.19.
Sun, C., Graff, M., and Liang, Y. (2017) Trace element partitioning between plagioclase and silicate melt: The importance of temperature and plagioclase composition, with implications for terrestrial and lunar magmatism. Geochimica et Cosmochimica Acta, 206, 273–295, https://doi.org/10.1016/j.gca.2017.03.003.
Wang, L.J., Guo, J.H., Yin, C., and Peng, P. (2017) Petrogenesis of ca. 1.95 Ga metaleucogranites from the Jining Complex in the Khondalite Belt, North China Craton: Water-fluxed melting of metasedimentary rocks. Precambrian Research, 303, 355–371, https://doi.org/10.1016/j.precamres.2017.04.036.
Wang, D., Liu, J., Carranza, E.J.M., Zhai, D., Wang, Y., Zhen, S., Wang, J., Wang, J., Liu, Z., and Zhang, F. (2019) Formation and evolution of snowball quartz phenocrysts in the Dongping porphyritic granite, Hebei Province, China: Insights from fluid inclusions, cathodoluminescence, trace elements, and crystal size distribution study. Lithos, 340-341, 239–254, https://doi.org/10.1016/j.lithos.2019.05.018.
Wang, P., Zhao, G., Liu, Q., Yao, J., Han, Y., and Li, J. (2022) Effect of source compositions on adakitic features: A case study from the Buya granite, in western Kunlun, NW China. American Journal of Science, 322, 828–850, https://doi.org/10.2475/06.2022.03.
Ward, R., Stevens, G., and Kisters, A. (2008) Fluid and deformation induced partial melting and melt volumes in low-temperature granulite-facies metasediments, Damara Belt, Namibia. Lithos, 105, 253–271, https://doi.org/10.1016/j.lithos.2008.04.001.
Waters, L.E. and Lange, R.A. (2015) An updated calibration of the plagioclase-liquid hygrometer-thermometer applicable to basalts through rhyolites. American Mineralogist, 100, 2172–2184, https://doi.org/10.2138/am-2015-5232.
Watkins, J.M., Clemens, J.D., and Treloar, P.J. (2007) Archaean TTGs as sources of younger granitic magmas: Melting of sodic metatonalites at 0.6–1.2 GPa. Contributions to Mineralogy and Petrology, 154, 91–110, https://doi.org/10.1007/s00410-007-0181-0.
Watson, E.B., Wark, D.A., and Thomas, J.B. (2006) Crystallization thermometers for zircon and rutile. Contributions to Mineralogy and Petrology, 151, 413–433, https://doi.org/10.1007/s00410-006-0068-5.
Weinberg, R.F. and Hasalová, P. (2015) Water-fluxed melting of the continental crust: A review. Lithos, 212-215, 158–188, https://doi.org/10.1016/j.lithos.2014.08.021.
Werts, K., Barnes, C.G., Memeti, V., Ratschbacher, B., Williams, D., and Paterson, S.R. (2020) Hornblende as a tool for assessing mineral-melt equilibrium and recognition of crystal accumulation. American Mineralogist, 105, 77–91, https://doi.org/10.2138/am-2020-6972.
Wieser, P.E., Jenner, F., Edmonds, M., Maclennan, J., and Kunz, B.E. (2020) Chalcophile elements track the fate of sulfur at Kīlauea Volcano, Hawai'i. Geochimica et Cosmochimica Acta, 282, 245–275, https://doi.org/10.1016/j.gca.2020.05.018.
Xie, Y.H., Li, X.W., Mo, X.X., Dong, G.C., Sun, Y.Q., and Shan, W. (2023) The effects of the source composition on the origin of orthopyroxene-bearing adakitic granitoid in West Qinling, Central China. Geoscience Frontiers, 14, 101554, https://doi.org/10.1016/j.gsf.2023.101554.
Xing, H., Li, X., Xu, J., Mo, X., Shan, W., Yu, H., Hu, J., Huang, X., and Dong, G. (2020) The genesis of felsic magmatism during the closure of the Northeastern Paleo-Tethys Ocean: Evidence from the Heri batholith in West Qinling, China. Gondwana Research, 84, 38–51, https://doi.org/10.1016/j.gr.2020.02.014.
Xu, X., Dong, C., Li, W., and Zhou, X. (1999) Late Mesozoic intrusive complexes in the coastal area of Fujian, SE China: The significance of the gabbro-diorite–granite association. Lithos, 46, 299–315, https://doi.org/10.1016/S0024-4937(98)00087-5.
Yang, Z.F., Luo, Z.H., and Lu, X.X. (2010) Quantitative textural analysis of igneous rocks and the kinetics and dynamics of magma solidification processes. Earth Science Frontiers, 17, 246–266.
Yu, S., Zhang, J., Qin, H., Sun, D., Zhao, X., Cong, F., and Li, Y. (2015) Petrogenesis of the early Paleozoic low-Mg and high-Mg adakitic rocks in the North Qilian orogenic belt, NW China: Implications for transition from crustal thickening to extension thinning. Journal of Asian Earth Sciences, 107, 122–139, https://doi.org/10.1016/j.jseaes.2015.04.018.
Zeng, L., Zhang, K., Tang, X., Zhang, Y., and Li, Z. (2018) Mid-Permian rifting in Central China: Record of geochronology, geochemistry and Sr-Nd-Hf isotopes of bimodal magmatism on NE Qinghai–Tibetan Plateau. Gondwana Research, 57, 77–89, https://doi.org/10.1016/j.gr.2017.12.013.
Zhan, Q.Y., Zhu, D.C., Wang, Q., Weinberg, R.F., Xie, J.C., Li, S.M., Zhang, L.L., and Zhao, Z.D. (2020) Source and pressure effects in the genesis of the Late Triassic high Sr/Y granites from the Songpan-Ganzi Fold Belt, eastern Tibetan Plateau. Lithos, 368-369, 105584, https://doi.org/10.1016/j.lithos.2020.105584.
Zhang, Y.Z., Wang, X.L., Li, J.Y., He, Z.Y., Zhang, F.F., Chen, X., Wang, S., Du, D.H., Huang, Y., and Jiang, C.H. (2021) Oligocene leucogranites of the Gangdese Batholith, Southern Tibet: Fractional crystallization of felsic melts from juvenile lower crust. Journal of Petrology, 62, egab076, https://doi.org/10.1093/petrology/egab076.
Zheng, J.P., Griffin, W.L., Sun, M., O'Reilly, S.Y., Zhang, H.F., Zhou, H.W., Xiao, L., Tang, H.Y., and Zhang, Z.H. (2010) Tectonic affinity of the west Qinling terrane (central China): North China or Yangtze? Tectonics, 29, https://doi.org/10.1029/2008TC002428.
Zhou, J., Wang, Q., Wyman, D.A., and Zhao, Z. (2020) Petrologic reconstruction of the Tieshan magma plumbing system: Implications for the genesis of magmatic-hydrothermal ore deposits within originally water-poor magmatic systems. Journal of Petrology, 61, egaa056, https://doi.org/10.1093/petrology/egaa056.

Manuscript received November 16, 2022
Manuscript accepted June 9, 2023
Accepted manuscript online June 21, 2023
Manuscript handled by Callum Hetherington

Endnote:

[1]Deposit item AM-24-48873. Online Materials are free to all readers. Go online, via the table of contents or article view, and find the tab or link for supplemental materials.